High resolution morphometric analysis of the Cordone del Vettore normal fault scarp (2016 central Italy seismic sequence): insights into age, earthquake recurrence and throw rates

S. Pucci[a], L. Pizzimenti[a], R. Civico[a], F. Villani[a], C. A. Brunori[a] and D. Pantosti[a]

[a]Istituto Nazionale di Geofisica e Vulcanologia, via di Vigna Murata 605, 00143 Rome, Italy.

Corresponding author: Stefano Pucci, stefano.pucci@ingv.it

Abstract

We investigated the late Quaternary throw distribution of the main normal fault that ruptured during the Mw 6.5 2016 earthquake in central Italy by means of a high-resolution structure-from-motion (SfM)-derived Digital Surface Model (DSM). We focused on a key area along the Cordone del Vettore fault (CDV), which is part of the Vettore-Bove fault system (VBFS). The CDV displays a prominent compound post-glacial scarp that allowed the reconstruction of the along-strike cumulative throw distribution. We propose a geometric approach to calculate the CDV fault throw distribution from the reconstruction of a displaced glaciation-related erosional surface, used as a geomorphic marker, and a series of closely spaced cross profiles. The proposed calculation accounts for both the slip vector direction and the degraded scarp top, including field data on fault dip angles. Following this approach, we recognized two scarps with a minimum average fault throw of ~21 m and ~35 m for this section of the investigated fault strand.

The correlation with the possible post-LGM (Last Glacial Maximum) deglaciation phases of the erosional surface suggests a minimum scarps age of 25-27 ka cal BP. Such age provides a reasonable CDV fault throw rate of ~0.8 mm/a, comparable with known long-term throw rates of the VBFS and active Apennines normal faults. By comparing the reconstructed long-term Cordone del Vettore throw distribution with the 2016 coseismic one, ~24 2016-like surface faulting events

are required to generate the main cumulative scarp, under the assumption of constant slip per event. This, along with the age of the scarp, yields an average earthquake recurrence time interval of ~1100 a. These results suggest the presence of multiple regional markers that correlates with different LGM (if not pre-LGM) major glacial phases, whose erosional processes allow the preservation the preservation of pre-existing bedrock fault scarp remnants.

Keywords: *morphometric analysis; structure-from-motion; fault scarp; active tectonics; earthquake; central Apennines.*

1. Introduction

Offset measurements of earthquake-generated landforms, either performed shortly after an earthquake or focusing on past earthquakes, contribute to the knowledge of how earthquakes generate surface deformation through seismic cycles and on how these contribute to landscape modelling (Wallace, 1977). Displacements recorded in the morphology, such as along fault scarps, are relevant in a number of applications for the assessment of future fault behavior (e.g., Wallace, 1968; Zielke et al., 2010 and 2012; Klinger et al., 2011; Salisbury et al., 2012; Benedetti et al., 2013; Manighetti et al., 2015; Ren et al., 2016), and in particular for the definition of fault activity over multiple earthquake cycles (i.e., defining slip accumulation models, e.g. Schwartz and Coppersmith, 1984; Friedrich et al., 2003), estimating maximum earthquake magnitudes through empirical scaling laws (e.g., Scholz et al., 1993; Wells and Coppersmith, 1994; Leonard, 2010; Stirling et al., 2013), or calculating fault slip rates in combination with Quaternary dating (e.g., McCalpin, 2009). Bedrock fault scarps along seismogenic normal faults have long been recognized worldwide as prominent features of the displaced landforms, for example, in Greece (e.g. Armijo et al., 1992), in the western United States (e.g., Teton, Wasatch, and Great Basin faults; Pierce and Good, 1992; Smith et al., 1993; Byrd et al., 1994; DePolo and Anderson, 2000; Smith and Siegel,

2000; Machette et al., 2001), and in southern Tibet (e.g. Armijo et al., 1986). These fault scarps represent a key archive of fault slip, since they are the cumulative result of repeated surface faulting earthquakes that progressively exhume previously unexposed slip surfaces, increasing the scarp height. The number of recorded episodes of coseismic displacement is a function of: 1) individual slip magnitude; 2) rupture recurrence time; 3) preservation potential of the scarp (i.e. mechanical properties of the substratum); 4) energy of the surface modeling processes. In the past two decades, these fault scarps have become attractive for investigations aiming to obtain slip-rates in Italy too (e.g. Piccardi et al., 1999; Morewood and Roberts, 2000; Giaccio et al., 2003; Roberts and Michetti, 2004; Papanikolaou et al., 2005; Faure Walker et al., 2009; Schlagenhauf et al., 2010), but also to reconstruct paleoseismic records and discuss segmentation and recurrence models (e.g. DuRoss et al., 2019).

In the central Apennines of Italy, where active extensional deformation is often associated with moderate to large (M > 5.5) earthquakes (e.g., D'Agostino, 2014), well-preserved Holocene bedrock fault scarps are assumed by most authors to represent long-term cumulated slip following the LGM (Last Glacial Maximum) (e.g. Bosi, 1975; Piccardi et al., 1999; Morewood and Roberts, 2000; Roberts and Michetti, 2004), even though some authors claim they are not entirely of tectonic origin but are mainly due to erosional processes (e.g. Kastelic et al., 2017). The assumption made by most authors is that the erosional processes acting on mountain slopes would have smoothed and even completely erased any pre-existing bedrock fault scarp. This is because bedrock fault scarps are characterized by hillslope erosion rate 30 times higher than in the Holocene when located at high altitude (>1000 m above sea level) in regions that experienced severe climatic conditions (from periglacial to nearly glacial) during the cold Pleistocene stages (Tucker et al., 2011). As a result, these processes provide a unique regional marker represented by

glaciation-related sediments and smoothed periglacial slopes (e.g. Giraudi, 1995). The age of this regional marker is commonly assumed to coincide with the last major glacial retreat phase (e.g. from Giraudi and Frezzotti, 1997; Allen et al., 1999). Because of this assumption, no pre-LGM fault scarp could be preserved in those environments. This assumption was tested only in recent times through a number of exposure-age cosmogenic ^{36}Cl dating of carbonate slip surfaces in the Apennines, performed on the lower part of the scarps (Benedetti et al., 2002 and 2003; Palumbo et al., 2004; Schlagenhauf et al., 2010 and 2011; Cowie et al., 2017; among others). The modeling of ^{36}Cl-derived slip profiles indicates scarps age ranging from ~10 ka to ~23 ka, with the mean of 17.8 ± 4.3 ka (Cowie et al., 2017). A single direct dating of preserved LGM hillslope exists at the footwall of the Fiamignano fault and yields an age of ~17 ka, confirming the initial hypothesis that these bedrock scarps record the cumulative fault slip since the demise of the LGM (Cowie et al., 2017).

Bedrock fault scarp investigations were recently improved by high-resolution Digital Elevation Models (DEMs) obtained from dense topographic point clouds acquired by means of LiDAR (Light Detection And Ranging) and photogrammetric range digital imaging processing (Structure-from-Motion - SfM - and Multi-View Stereo - MvS; Gallup et al., 2007; Goesele et al., 2007; Jancosek et al., 2009; Westoby et al., 2012) (Frankel et al. 2007 and 2016; Brunori et al., 2012; Howle et al., 2012).

The surface-faulting from the 30 October 2016, Mw 6.5 Norcia earthquake in central Italy, demonstrated that seismic slip of large shallow crustal earthquakes plays a major role in the genesis of the central Apennines bedrock fault scarps (e.g. Villani, Pucci et al., 2018), and provides a unique opportunity to compare the coseismic and long-term expressions of the Mt. Vettore - Mt. Bove fault system (VBFS). In this work, we focus on the key area of the Cordone del Vettore fault

(hereinafter CDV), which ruptured in 2016 and that exhibits a prominent cumulative fault scarp. We reconstruct the along-strike, long-term (i.e. Late Pleistocene) throw distribution curve, in order to provide insights into both throw rate and average recurrence interval of this fault splay of the VBFS. With this aim, we integrated existing structural data (Villani, Pucci et al., 2018) with a new geological field survey and reconstructed high-resolution digital surface model (DSM), by means of the 3D photo-based SfM-MvS algorithm (James and Robson, 2012; Westoby et al., 2012; Fonstad et al., 2013; Johnson et al., 2014; Bemis et al., 2014; among others). We analysed this DSM through the development and application of an original fine-scale quantitative approach for the throw calculation. Then, we correlated a glaciation-related marker (i.e., smoothed periglacial slope - e.g. Giraudi, 1995), displaced by the CDV cumulative scarp, with the ages of the different deglaciation phases of the Apennines post-LGM, whose chronology was recently updated by Giraudi (2015). Finally, we used the obtained results to provide plausible estimates of the Late Pleistocene long-term CDV throw rate and speculate on average earthquake recurrence time. We discuss most of these estimates by comparison with those obtained by means of other approaches along the VBFS and from other active faults of the central Apennines.

2. Geological Background and Seismotectonic Framework

The 2016-2017 seismic sequence hit an area located in the axial portion of the central Apennines, a Neogene NE-verging fold-and-thrust orogen, whose evolution is characterized by the eastward migration of its compressional front (see Carminati and Doglioni, 2012 for a review). Post-orogenic, late Pliocene-Quaternary crustal extension affected the Apennines (Lavecchia et al., 1994; Cavinato and De Celles, 1999; Ghisetti and Vezzani, 1999; D'Agostino et al., 2001), overprinting previous compressional structures (Vai and Martini, 2009; Vezzani et al., 2010;

among others). Miocene-Pliocene thrusting and Pliocene-Quaternary normal faulting, accompanied by large-scale uplift (D'Agostino et al., 2001; D'Anastasio et al., 2006), contributed to building the rugged and elevated topography of the area (up to ~2,500 m above sea level - a.s.l.) with reliefs locally exceeding 1,000 m.

The central Apennines undergo ~1.5-3 mm/a, NE-trending regional extension (Serpelloni et al., 2005; D'Agostino et al., 2008; Faure Walker et al., 2010), which acted with the same rate for at least the past 15 ± 3 ka (Faure Walker et al., 2012). This extension is accommodated by a dense array of NW- and NNW-striking, mainly SW dipping, 20-30 km-long active normal fault systems with throw rates of 0.3-2.0 mm/yr ka (Barchi et al., 2000; Galadini and Galli, 2000; Morewood and Roberts, 2000; Cowie and Roberts, 2001; Tondi and Cello, 2003; Roberts et al., 2004; Pizzi and Galadini, 2009). Such active normal fault systems controlled onset, geometry and sedimentation rate of several intermontane continental basins (Blumetti et al., 1993; Cello et al., 1997; Cavinato and De Celles, 1999; Bosi et al., 2003; Galli et al., 2005; Blumetti and Guerrieri, 2007). The active extension of the area is testified by the occurrence of a series of historical and instrumental moderate ($5 < M < 6$) to large (up to M ~7) normal faulting earthquakes (Rovida et al., 2016; Fig. 1), typically defining a relatively shallow seismogenic thickness (5-15 km) (Chiarabba et al., 2005; Mirabella et al., 2008; Chiarabba and Chiodini, 2013). Historical documentation and fault-specific paleoseismological investigations support the occurrence of past coseismic surface faulting for several earthquakes (e.g., Mw 6.9-7.0, 1915 Avezzano - Oddone, 1915; Serva, et al., 1988; Michetti, et al., 1996; Galadini and Galli, 1999 -; Mw 6.0, 1997 Colfiorito - Basili et al., 1998; Cinti et al., 1999; Cello et al., 2000; Mildon et al., 2016 -; and Mw 6.1, 2009 L'Aquila - e.g.: Boncio et al., 2010; EMERGEO Working Group, 2010; Vittori et al., 2011). The

average earthquake recurrence times is in the order of hundreds to thousands of years (Blumetti., 1995; Pantosti et al., 1996; Galadini and Galli, 2003; Galli et al., 2008).

With regard to the ~25-30 km-long Mt. Vettore-Mt. Bove and the 30 km-long Laga Mountains fault-systems (VBFS and LMFS hereafter), previous studies pointed out their seismogenic potential (Galadini and Galli, 2003; Boncio et al., 2004) highlighted by an apparent lack of significant seismicity and concurrent clear geomorphic evidence of Holocene active faulting (Calamita et al., 1992; Calamita and Pizzi, 1992; Calamita and Pizzi, 1994; Lavecchia et al., 1994; Galadini and Galli, 2000). The VBFS, in particular, dissects the western slope of the Sibillini Mountain range through several, parallel NNW-SSE trending splays, both synthetic and antithetic, affecting the more resistant carbonate units of the Umbro-Marchean, Meso-Cenozoic multilayer (Fig. 1) (e.g. Koopman et al., 1983; Lavecchia, 1985; Pierantoni et al., 2005). The VBSF paleoseismic record indicates at least seven M□6.5 surface-faulting events in the past ~22 ka, with an average recurrence time of 3,360-3,640 years (1,220-1,970 years for the last ~4 ka) and a dip-slip rate of 0.26-0.38 mm/a, to be considered as minimum since it was evaluated on a single fault splay of a wide zone of deformation (Galli et al., 2019; Cinti et al., 2019).

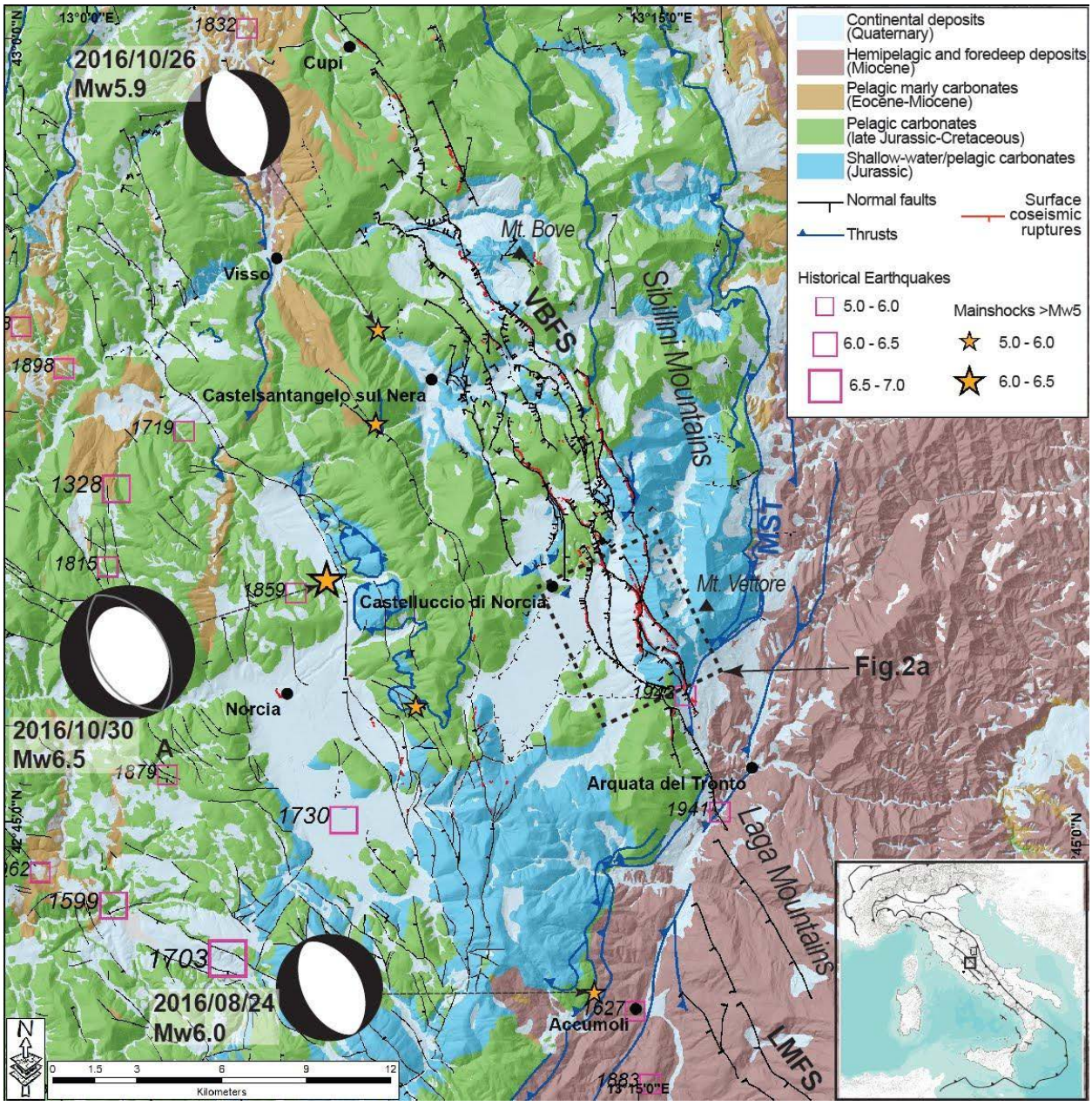
13°0'0"E
13°15'0"E
43°0'0"N
42°45'0"N
2016/10/26
Mw5.9
2016/10/30
Mw6.5
2016/08/24
Mw6.0
1832
Cupi
Visso
1898
Castelsantangelo sul Nera
1719
1328
1815
1859
Castelluccio di Norcia
Norcia
1879
1730
1599
1703
1627
Accumoli
1883
Mt. Bove
Mt. Vettore
1972
Arquata del Tronto
1941
VBFS
Sibillini Mountains
MSF
Laga Mountains
LMFS
Fig.2a
A
Continental deposits (Quaternary)
Hemipelagic and foredeep deposits (Miocene)
Pelagic marly carbonates (Eocene-Miocene)
Pelagic carbonates (late Jurassic-Cretaceous)
Shallow-water/pelagic carbonates (Jurassic)
Normal faults
Thrusts
Surface coseismic ruptures
Historical Earthquakes
5.0 - 6.0
6.0 - 6.5
6.5 - 7.0
Mainshocks >Mw5
5.0 - 6.0
6.0 - 6.5
N
0 1.5 3 6 9 12
Kilometers

Figure 1. Simplified geological map of the area struck by the 2016-2017 seismic sequence (compiled from 1:10,000-scale cartography of Regione Umbria and Marche, Centamore et al., 1992, and Pierantoni et al., 2013). The labels VBFS and LMFS indicate the Mt. Vettore-Mt. Bove and Laga Mts. fault systems, respectively. MST indicates the Sibillini Mts. thrust. The pink open squares indicate the main historical seismic events (Guidoboni et al., 2018). The time-domain moment tensor solutions of the Mw 6.5 mainshock on 30 October 2016 and of the two other mainshocks on 24 August and 26 October 2016 are from Scognamiglio et al. (2018), Tinti et al. (2016), and Chiaraluce et al. (2017), respectively. The trace of the coseismic surface ruptures produced by the three mainshocks (in red) is compiled from Civico et al. (2018) and Brozzetti et al. (2019).

Based on displacements evaluated through geological cross-sections (Pizzi et al., 2002; Porreca et al., 2020) and geophysical investigations (Villani et al., 2019), the aggregate VBFS maximum stratigraphic throw is ~1400 m and translates into long-term slip rates of 0.7-1.4 mm/a. Such slip rates are deduced from the hypotheses of no pre-orogenic extension contributing to the net displacement and of post-orogenic onset of extension at 1.0-2.0 Ma (Cavinato and De Celles, 1999). The throw maximum is located in the southern part of the fault system, along the western slope of the Mt. Vettore, where the CDV fault splay appears as a prominent bedrock fault scarp at the surface (Fig. 2a). This splay contributes to the aggregate VBFS net stratigraphic and topographic throws with maxima of 470 m and 25 m, respectively (Brozzetti et al., 2019).

2.1. The 2016 surface rupture

The Amatrice-Visso-Norcia 2016-2017 seismic sequence reactivated the VBFS and LMFS adjacent active normal fault systems (Fig. 1). The three largest mainshocks of the sequence nucleated at a depth of ~4.0-8.0 km (Tinti et al., 2016; Chiaraluce et al., 2017; Scognamiglio et al., 2018; Improta et al., 2019): 1) the 24 August 2016 Mw 6.1 earthquake epicenter was located south of the VBFS; 2) the 26 October 2016 Mw 5.9, was located in the northernmost part of the VBFS,

close to Visso; and 3) the 30 October Mw 6.5, occurred close to Norcia, in between the two previous events, and was the largest shock of the sequence (Fig. 1).

Coseismic surface ruptures were observed following the 24 August Amatrice earthquake for a minimal length of ~5–6 km along the southernmost part of the VBFS, at the base of the CDV and Mt. Vettoretto cumulative fault scarp (Fig. 2a), with average surface slip of ~0.13 m and local peaks >0.30 m (Emergeo Working Group, 2016; Livio et al., 2016; Pucci et al., 2017).

The 26 October 2016 Visso earthquake caused only sparse and discontinuous (each up to a few hundred of meters long) ground ruptures for a minimum total length of about 7.0 km along the northernmost part of the VBFS, with an average surface slip of ~0.11 m and a peak of 0.40 m (EMERGEO Working Group, 2017; Pizzi et al., 2017; Villani, Pucci et al., 2018; Brozzetti et al., 2019).

Surface ruptures of the 30 October Norcia event as a whole were significantly longer (nearly 22-km long) and more continuous, and involved almost the entire length of the VBFS. These overprint the ruptures of the Amatrice earthquake and part of the Visso earthquake ruptures, and displayed an average surface slip of ~0.44 m and a peak of 2.10 m located along the CDV splay, where most of the surface slip occurred (Civico et al., 2018; Villani, Civico et al., 2018; Villani, Pucci et al., 2018; Brozzetti et al., 2019). Worthy to note, the locus of maximum surface slip corresponds to a large slip patch (~3 m) evidenced by models of the 2016 fault slip distribution at depth, as inferred from the inversion of seismological and geodetic data (e.g. Scognamiglio et al., 2019; Walters et al., 2018). Coseismic offset across surface ruptures was measured with some near-field 1-Hz Global Navigation Satellite System stations, revealing that the ruptures formed before the onset of local peak ground acceleration, thus definitively supporting their primary tectonic origin (Wilkinson et al., 2017).

Collectively, the 2016 sequence surface coseismic ruptures extend from the village of Ussita to Arquata del Tronto, roughly striking ~N155° for a minimum length of ~28 km. The ruptures affect the entire VBFS with a complex pattern, running along several distinct SW-dipping (synthetic) and NE-dipping (antithetic) splays that, for the most part, are associated with previously mapped long-term cumulative fault scarps, and occurred along bedrock fault planes. The coseismic surface throw curve obtained with moving average windows, displays a systematic increase from the NW to the SE, reaching a peak of ~100 cm along the CDV fault splay where it includes both August, the 24th and October, the 30th 2016 events (Villani, Civico et al., 2018; Brozzetti et al., 2019).

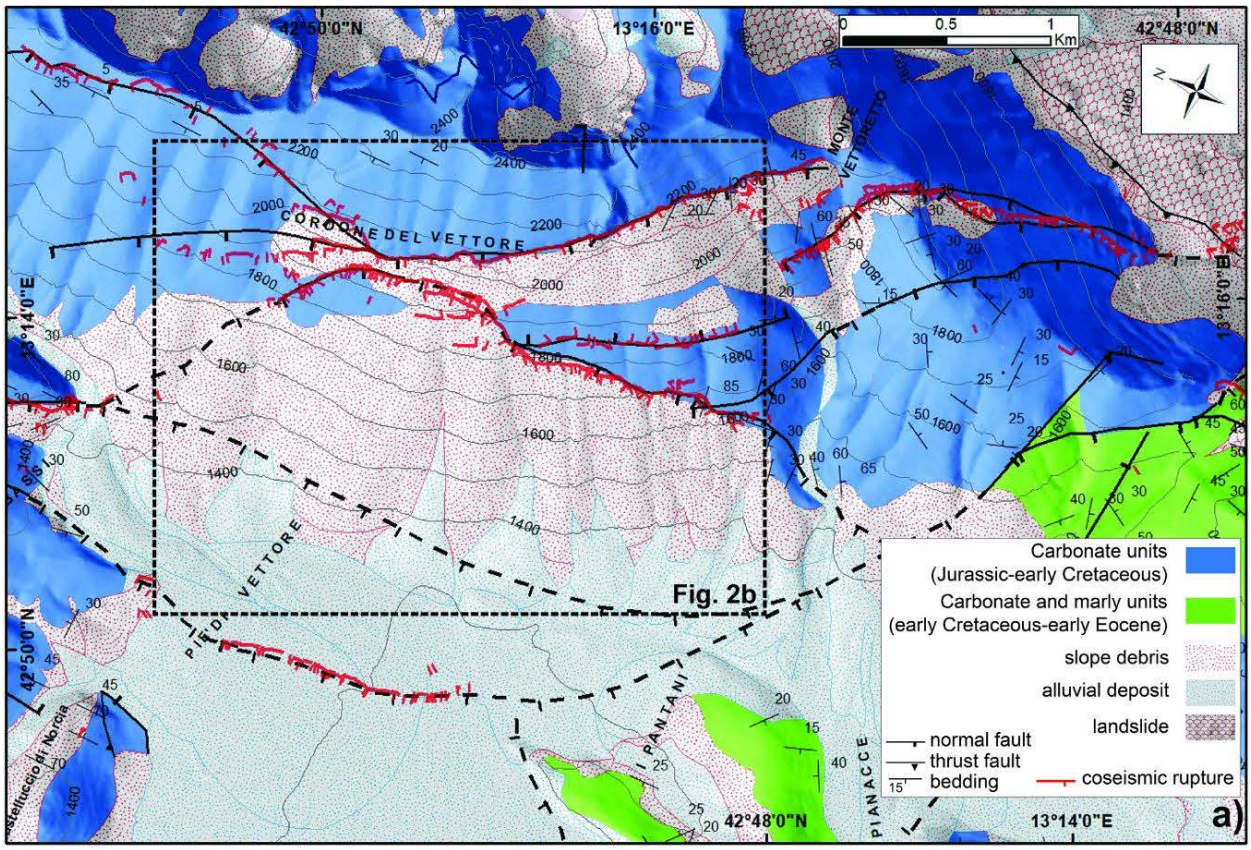
42°50'0"N
13°16'0"E
42°48'0"N
13°14'0"E
0 0.5 1 Km
N
CORDONE DEL VETTORE
MONTE VETTORETTO
PIEDI VETTORE
I PIANTANI
PIANACCE
Fig. 2b
Carbonate units (Jurassic-early Cretaceous)
Carbonate and marly units (early Cretaceous-early Eocene)
slope debris
alluvial deposit
landslide
normal fault
thrust fault
bedding
coseismic rupture
a)

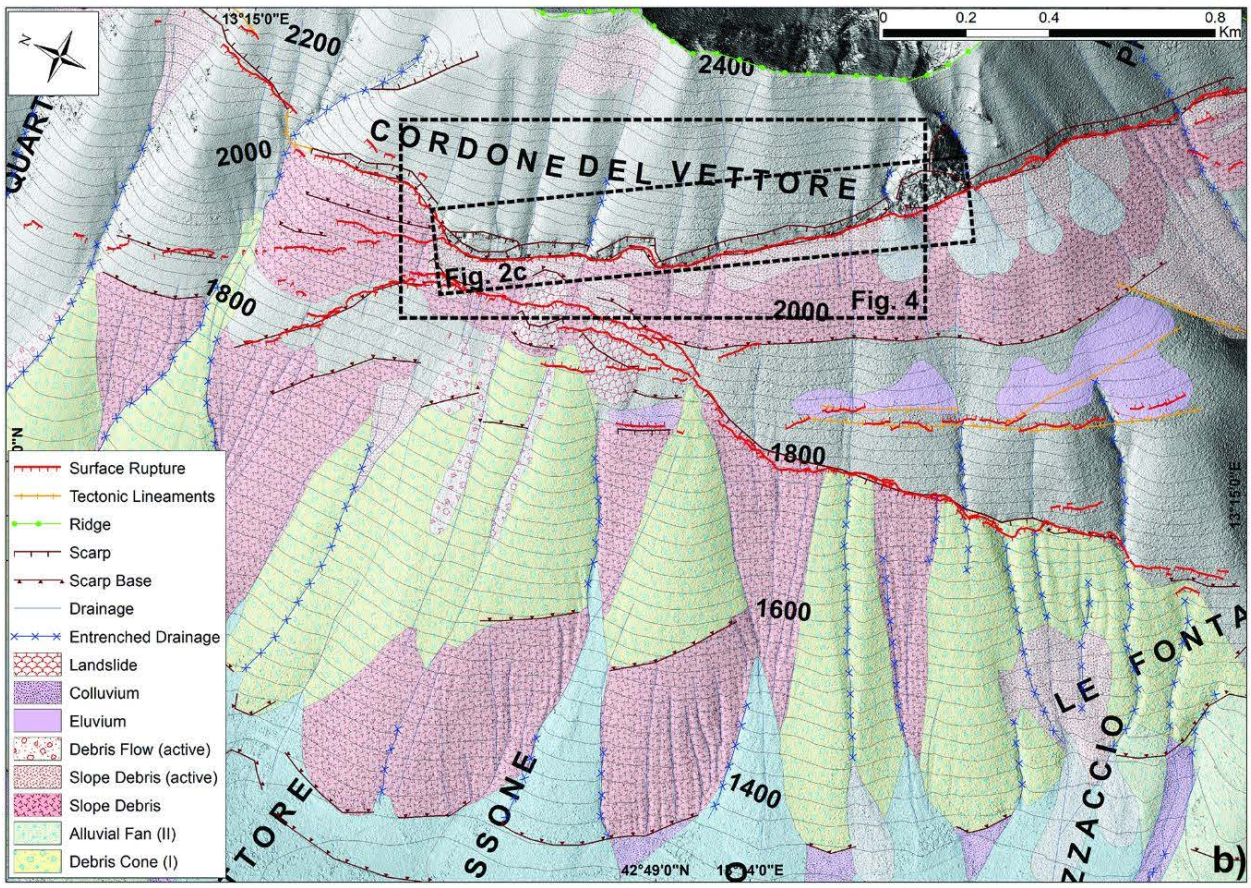
13°15'0"E
0 0.2 0.4 0.8 Km
N
CORDONE DEL VETTORE
Fig. 2c
Fig. 4
Surface Rupture
Tectonic Lineaments
Ridge
Scarp
Scarp Base
Drainage
Entrenched Drainage
Landslide
Colluvium
Eluvium
Debris Flow (active)
Slope Debris (active)
Slope Debris
Alluvial Fan (II)
Debris Cone (I)
42°49'0"N
b)

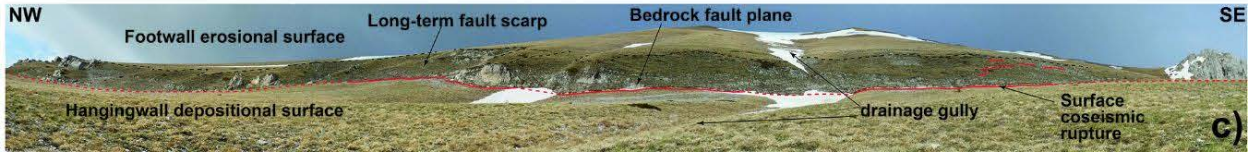
NW
SE
Footwall erosional surface
Long-term fault scarp
Bedrock fault plane
Hangingwall depositional surface
drainage gully
Surface coseismic rupture
c)

Figure 2. The Cordone del Vettore fault scarp. **a)** Simplified geological map of the western flank of Mt. Vettore affected by the southern portion of the Mt. Vettore-Mt. Bove fault system (compiled from 1:10,000-scale cartography of Regione Umbria and Marche, Centamore et al., 1992, and Pierantoni et al., 2013). The trace of the 2016 coseismic surface ruptures is compiled from Civico et al. (2018) and Brozzetti et al. (2019); **b)** Geomorphological map of the western flank of Mt. Vettore derived from the interpretation of aerial photo stereo pairs (Istituto Geografico Militare, G.A.I. 1955) and 0.5-m resolution DEM (from Pleiades satellite optical images; Delorme et al., 2020). See Fig. 2a for location; **c)** Panoramic view of the SW-facing CDV fault scarp. See Fig. 2b for location.

3. Data and methods

3.1. The CDV scarp

The prominent ~4.0 km-long, SW-facing CDV fault scarp interrupts the geomorphologic continuity of the southwestern, NNW–SSE-trending slope of Mt. Vettore between 2000 and 2200 m a.s.l. (Fig. 2). As a first step, we performed a geomorphological analysis of the CDV fault scarp through the interpretation of aerial photo stereo pairs (G.A.I. 1955) and 0.5-m resolution DEM (from Pleiades Orthophoto; Delorme et al., 2020) that highlighted a complex pattern of slope shaping processes. The CDV fault juxtaposes Jurassic carbonate units at the footwall with Quaternary continental deposits on the hangingwall (Fig. 2a). Erosional processes affect the footwall, whereas the hangingwall is dominated by both ancient and active slope debris and debris flows emplacements (Fig. 2b and c). In detail, the footwall slope displays an erosional surface locally dissected by gullies, cutting into the underlying Jurassic carbonate units (dip directions N271° to N181°, dip angles ~20°; Fig. 2a). Conversely, the CDV fault hangingwall displays widespread deposition of debris from the footwall erosion, mostly by means of cryoclastic processes driven by the periglacial conditions affecting the Apennines summit areas during the Late Pleistocene-Holocene (Giraudi, 2004 and 2015). In proximity to the base of the CDV fault

scarp, angular clast-supported and poorly-sorted active slope deposits spread out, forming a steep (26°-30°) detrital apron. The hangingwall slope gradient progressively decreases approaching the local base level (i.e. Castelluccio di Norcia Plain, ~1300 m a.s.l.), through a system of prograding depositional bodies of both active and inactive debris cones and alluvial fans, along with the emplacements of active debris flows (Fig. 2b).

3.2. SfM workflow

A high-resolution digital surface model (DSM) of the CDV fault scarp was reconstructed by means of digital photogrammetric techniques (SfM and MvS). The workflow started with the acquisition of oblique aerial photographs (more than 11,000 digital images) taken from six helicopter flights, for a total of 12 hours flight (November 22nd and 23rd 2016). This was particularly useful as the survey target was located in a scarcely accessible and, in places, dangerous area. Oblique photographs were taken from two handheld cameras equipped with the same 24-megapixel APS-C CMOS sensor (Sony ILCE-5100 and Nikon D5300) capable of a maximum resolution of 6000 x 4000 pixels. Photographs were acquired as raw image files (*.arw and *.nef) using focal lengths variable from 24mm to 75mm (35mm equivalent focal length). Each photo was therefore associated with its own geographical coordinates (latitude, longitude and altitude) using track files recorded with an external GPS receiver. Raw image files were converted to Digital Negative (DNG) files and homogenized in tonal values (e.g. brightness, contrast) by means of Adobe Lightroom® software.

Following image acquisition, we collated a photoset of 479 images on the basis of quality and framing. We processed the georeferenced images using the Agisoft Photoscan Pro® (v. 1.4.5) by means of the photogrammetric digital imaging processing (Fonstad et al., 2013; James and

Robson, 2012). The analysis included: 1) camera triangulation, with image position and orientation, and generation of sparse point cloud; 2) generation of dense points clouds and 3) generation of digital orthophotographs (DOP) and DSM extraction. We set processing parameters in Agisoft Photoscan Pro® to get high accuracy and quality for both photo alignment and dense point cloud, respectively. Then, using the DEM generation tool in Agisoft Photoscan Pro® (inverse-distance weighting method), we converted our point clouds into a 0.15 m/pixel DSM for a 1700-m long, 500-m wide portion of the CDV fault scarp (Fig. 3). As a last step, we compute slope information from the DSM by means of the standard ArcGIS tool. A slope map was generated from a DSM resampled to 0.5 m/pixel in order to filter slope values related to the presence of anti-dip slope bedding of outcropping bedrock layers, up to 0.4 m thick. The slope map identifies the rate of maximum change in z-value from each cell and is calculated in degrees, from 0° (horizontal) to 90° (vertical).

The main source of error in our DSM results from a complex interplay of factors such as camera calibrations, image overlap, ground sample distance and ground-control target recognition, and GNSS RTK (Global Navigation Satellite System, Real Time Kinematic) measurement. In order to reduce the error and to avoid motion blur, we used camera shutter speeds (i.e. exposure times) between 1/320 and 1/200, and we placed a network of 16 ground-control points (GCPs). GCPs markers were measured in the field using GNSS RTK positioning technique (Leica Geosystem GX1230GG and antenna AX1202GG). The markers were positioned in the field at unambiguous and in plain sight reference points in order to be clearly recognizable on the images and were then used to scale and orient the point cloud (see Tab. S1 in Supplementary material). We are aware of the non-optimal spatial distribution of the GCPs due to: 1) the paucity of clearly identifiable targets in the upper portion of the CDV fault scarp and 2) the limited accessibility of

some portion of the CDV fault scarp. The elevation accuracy of the resulting DSM was evaluated as the misfit in elevation between the GCPs and the DSM and resulted in a mean elevation difference of -0.09 m and a median elevation difference of -0.03 m.

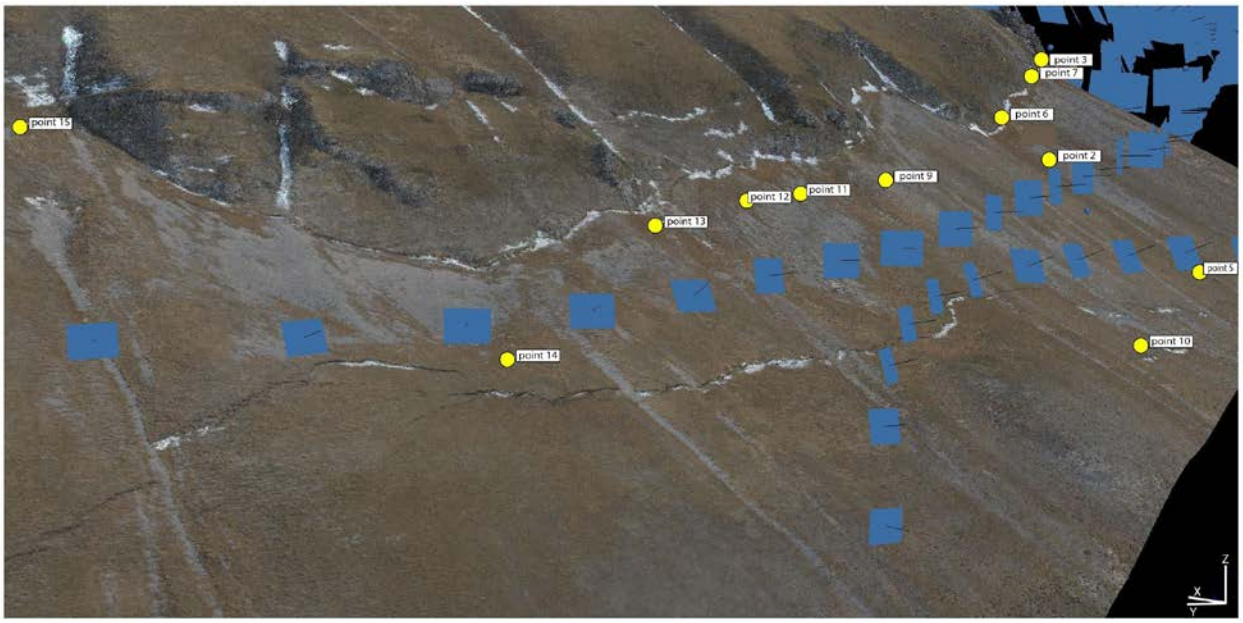

Figure 3. Oblique view (SE-looking) of the 3D SfM model of the CDV fault scarp. Blue squares represent aerial photo shooting point and orientation. Labeled yellow points mark the location of GCPs.

3.3. Measurement of fault scarp morphologic throw

The morphologic throw of the CDV cumulative fault scarp was calculated using the DSM along a ~1.0 km-long portion selected on the basis of its clear continuity and freshness. In fact, this scarp portion appears affected by few non-tectonic processes that may have degraded the scarp morphology (e.g. channel incision, sediment accumulation, landsliding) (Fig. 4). The DSM-derived slope map facilitated the identification of the fault scarp and its constituent features (Fig. 4b). The scarp was subdivided in two NW-SE oriented sectors (400 to 480 m long) on the basis of aspect variations (Sectors 1 and 2, striking N167° and N144°, respectively). To constrain the

continuity of the footwall erosional surface, the sectors extend ~200 meters upslope with respect to the morphologic scarp.

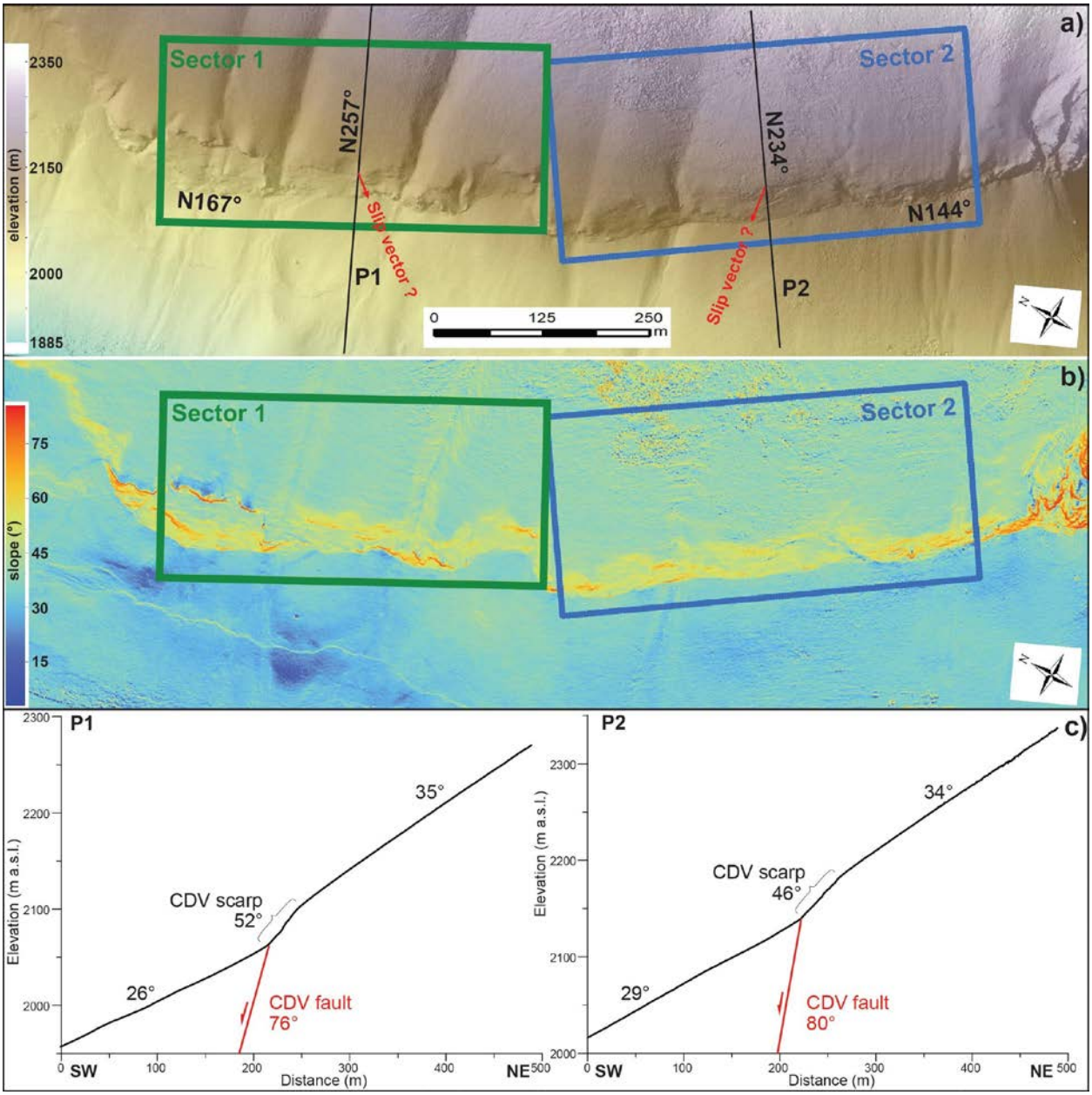

Figure 4. Shaded relief from the Digital Surface Model (**a**) and derivative Slope Map (**b**) of the CDV fault scarp study area reconstructed through the Structure-from-Motion technique. Green and blue rectangles enclose the two sectors of analysis. See figure 2b for location. **c**) Topographic profiles across CDV fault scarp at Sector1 (P1) and Sector2 (P2). Slope angles of footwall, hangingwall and escarpment are reported along with the CDV fault dip angle. Location in Fig. 4a.

In general, the CDV flank shows a well-preserved bedrock erosional surface (possibly LGM marker), at the footwall, and a sequence of large detrital aprons (unconformably stacked and topped by a thin post-LGM talus), at the hangingwall (Fig. 5a). The footwall and hangingwall present different steep slopes (~26-30° and ~28-37°, respectively), with a topographic gradient that sharply changes in coincidence with the fault scarp (Figs. 4 and 5a). Here, the scarp slope is shallower than the fault plane dip angle, suggesting a degraded bedrock fault scarp that is composed of a steep lower scarp, occasionally due to the exposed bedrock fault slickensides and a smoothed upper scarp (Fig. 4c and 5a).

Considering the footwall erosional surface as a geomorphologic marker offset by the CDV fault, the homologous morphological element at the hangingwall could be represented by a LGM basal unconformity of a detrital apron (Fig. 5a). Hence, it is not possible to project on the fault surface the topographic profiles from both walls to get their vertical separation (e.g. Bucknam and Anderson, 1979). For this reason, to calculate the post-LGM tectonic offset from the scarp profile, we assume that: i) the erosional surfaces exposed at the fault footwall and the buried unconformity at the hangingwall were originally coeval, continuous, and quasi-planar, and were subsequently faulted; ii) the erosional surface weathering was mostly negligible (with the exception of local downcutting exerted by the linear incisions- i.e. gullies) in comparison to fault slip rate; iii) the footwall erosional surface cut-off was eroded due to the upper fault scarp degradation; iv) the hangingwall unconformity cut-off lays directly below a thin debris talus with wedge shape and proximal detrital apron thickness approaches zero at the scarp base (conservative assumption in terms of amount of offset calculation). This assumption is possible because, given the steep slope setting, the reworking processes in the hangingwall produced an efficient down-slope sediment removal via debris flows (see Fig. 2b and Fig. 5a).

For each profile, the minimum vertical component of the offset was calculated identifying the eroded footwall erosional surface cut-off from the intersection of two straight lines: 1) the envelope of the footwall surface; and 2) the updip projection of the measured fault plane. The solution of the equations of the two non-parallel lines from the common coordinates of the intersection point (i.e. footwall cut-off), is provided through the formula (Eq. 1):

$$z = S/(1-tg\gamma/tg\alpha) \quad (1)$$

Where: z is the minimum vertical separation (minimum throw T when calculated along the fault slip vector, e.g. Fig. 4a); surface offset (S) and γ are the intercept with the vertical axis and the slope angle, respectively, of the footwall erosional surface line; α is the slope angle of fault plane line (Fig. 5b). A linear best fit (i.e. regression line) of the elevation points defining the footwall erosional surface trend is used to derive the slope angle (γ) and the surface offset S. As a dip angle of the fault plane (α) we used, for each profile, the nearest bedrock fault slickensides measured in the field (~90 measurements along the two sectors).

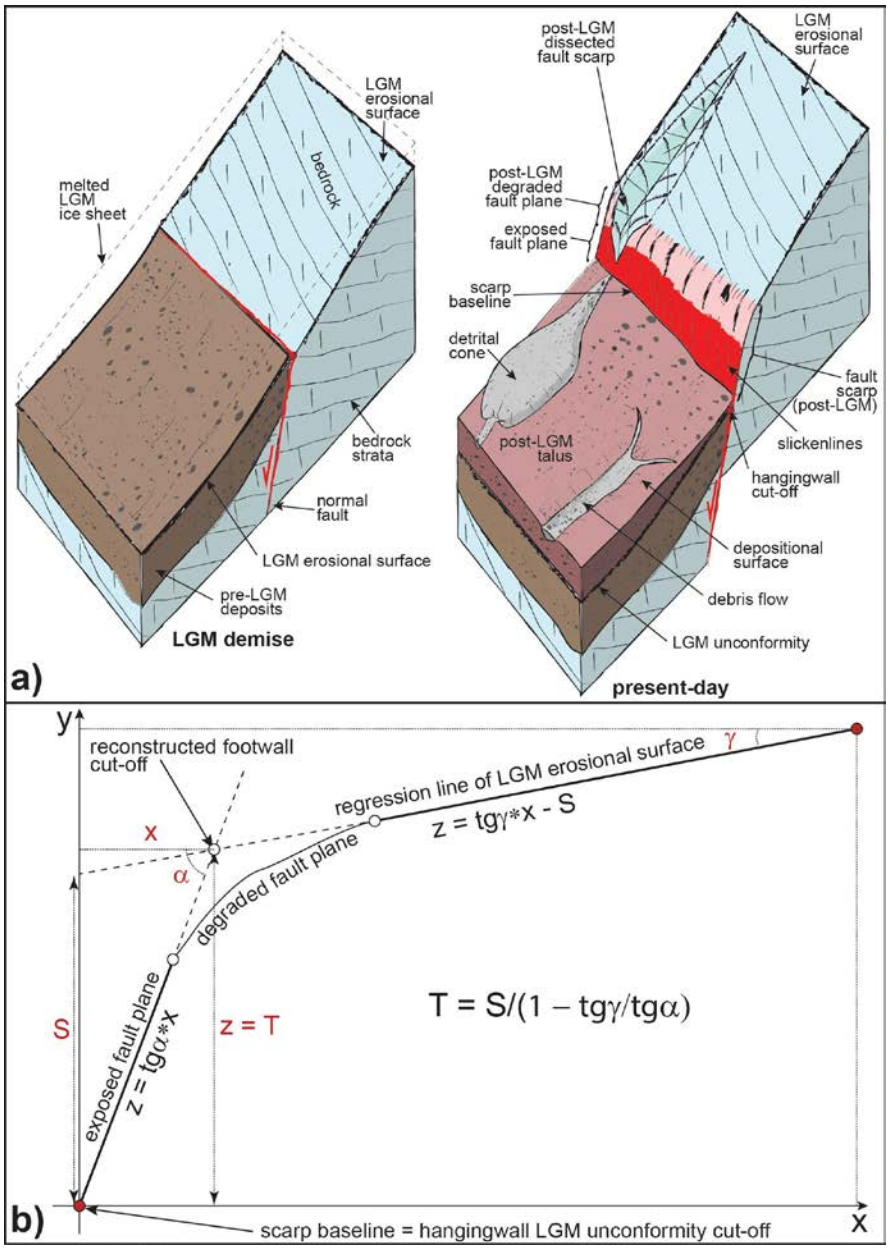

Figure 5. a) Conceptual block diagrams of the CDV steep slopes during the demise of the last glacial maximum (LGM) and present-day. At the demise of the LGM, the hypothesis is that the CDV slope was originally quasi-planar and the scarp was generally not exposed as erosion and sedimentation rates outstripped the fault slip rate. At present day, the CDV scarp records the post-LGM fault slip; **b)** Conceptual topographic profile showing the vertical separation (z) calculation method (z = throw T if along the fault slip vector). The equations of the two non-parallel lines used to reconstruct the footwall cut-off are reported: γ is the slope angle of the footwall erosional surface at the top of the scarp identified by the regression line; surface offset (S) is its intercept with the vertical axis; α is the dip angle of the fault plane.

A total of 864 parallel, 1-m spaced topographic profiles were extracted from the SfM-derived DSM and traced perpendicular to the average scarp strike of each sector (N257° and N234°, for profiles of Sector 1 and 2, respectively) (Fig. 6) (see Supplementary material S2 for details on data extraction workflow). The abrupt slope change discontinuity at the base of the scarp was set as origin (i.e. baseline) of the profiles. Slope and elevation values were sampled along each profile at 0.5 m spacing. The output dataset of profiles (Supplementary material, S2) contains the following parameters: profile number, point number per profile, distance along scarp baseline, absolute position, absolute elevation, relative elevation (elevation changes with respect to the baseline), down-dip slope angle (deriving from the corresponding pixel of the resampled DSM), slope angle of the footwall erosional surface (γ), coefficient of determination (R^2) for the regression lines approximating the erosional surface, standard error of γ, surface offset (S), assigned α, calculated vertical separation (z), calculated minimum throw (T). The sectors 1 and 2 cover 65,000 and 69,000 m^2, respectively with a grid spacing of 1.0×0.5 meters.

To obtain the minimum net geological throw (T) of the CDV fault scarp, we calculated the vertical separation (z) along the best-fit slip vector of each scarp sector. As a first step, we compared the 2016 coseismic kinematic strain field (by means of linked Bingham statistical analysis through FaultKin v.8.1 software from Allmendinger et al., 2012; data on bedrock fault planes from Villani, Civico et al., 2018) and the collected long-term kinematic indicators (i.e. slickenlines, rock and calcite striae measured on bedrock slickensides). Then, the best-fit slip vector, along with the fault plane solution, was computed through Stereonet v.11 software (Allmendinger et al., 2012). Finally, the long-term distribution curve of the CDV throw was compared with the coseismic 2016 one (from Villani, Pucci et al., 2018).

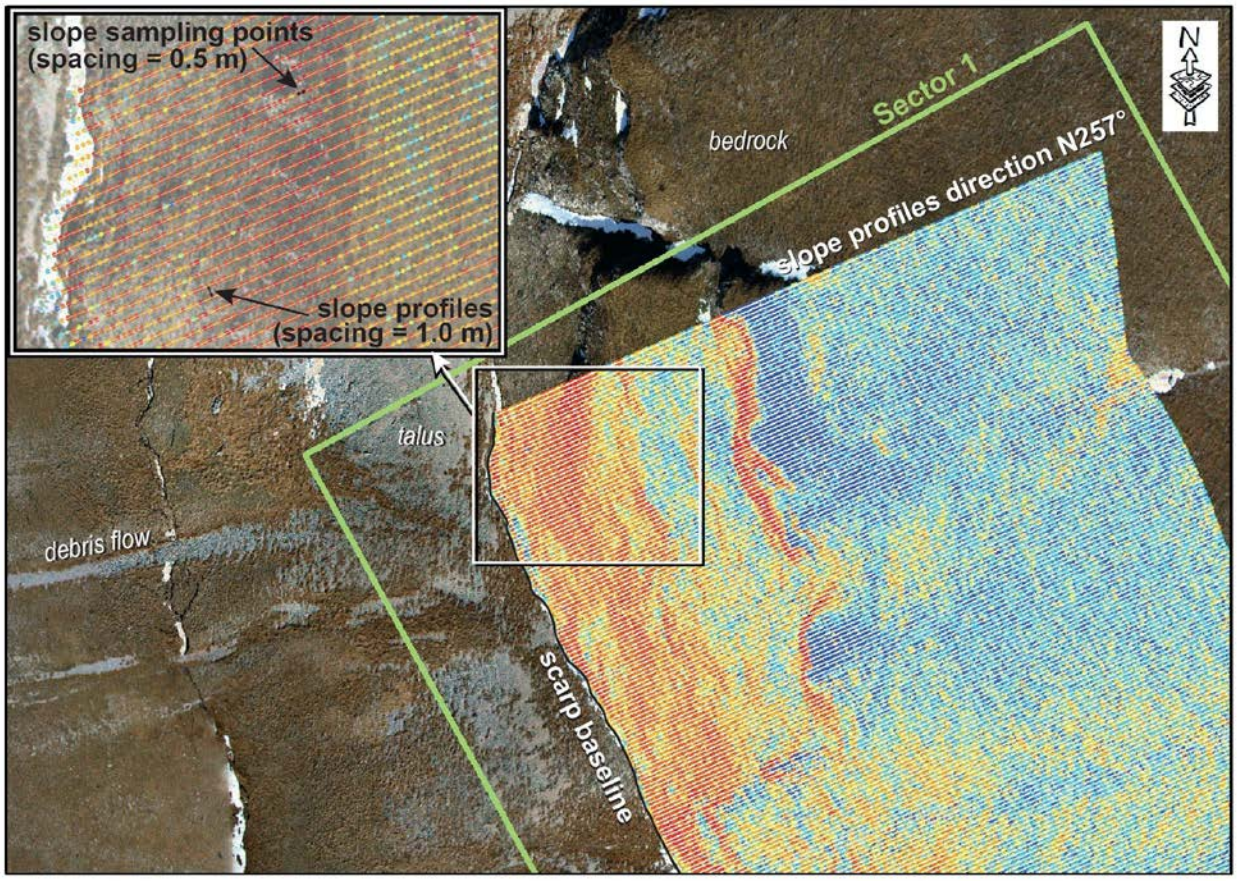

Figure 6. Close up of the northern side of Sector 1. The profiles, perpendicular to the scarp baseline, are composed by sampling points colour coded according with the slope angle. The reconstructed DOP is shown as a basemap.

In general, due to the epistemic uncertainties and assumptions affecting the studied geomorphic marker (e.g. original geometry, genetic process, age, grade of preservation, throw distribution in space and time, etc.), the formal errors are optimistic with respect to the inherent aleatory uncertainties. For this reason, we propose that the numbers provided, as far as accurate, should be considered as an approximation useful for general considerations and/or for comparisons.

4. Results

4.1 Morphological features of the CDV scarp

The SfM-derived DSM allowed us to analyse a significant portion of the CDV bedrock fault scarp (Fig. 7). At the CDV footwall we recognized and reconstructed a bedrock erosional surface presenting a general continuity and an average slope angle of 33° and 35° for Sector 1 and Sector 2, respectively. Sector 1 displays three gullies incising the bedrock erosional surface, disappearing upslope (i.e. smooth gully heads) and feeding active channelized debris flows in the hangingwall. Conversely, Sector 2 shows a lower degree of erosion with several weak linear incisions. The footwall gully erosion shows a continuity across the CDV scarp, incising also the loose slope deposits along the hangingwall, denoting here an active incision that recently (Holocene?) overtook the deposition. In general, due to its steepness, the Mt. Vettore southwestern slope presents a very low drainage connectivity (i.e. separated runoff paths) and appears to be weathering-limited (*sensu* Carson and Kirkby, 1972), with regolith of the CDV footwall being removed as fast as it is produced.

The high-resolution DSM displays slight differences in the morphological characteristics of the two CDV scarp sectors. Sector 1 presents a compound scarp composed of two sub-parallel elements; a downward concavity that interrupts the scarp linearity to the southeast (Fig. 7a), possibly representing a landslide crown related to a partial gravitational collapse of the footwall. Sector 2 presents a single and rectilinear scarp (Fig. 7b).

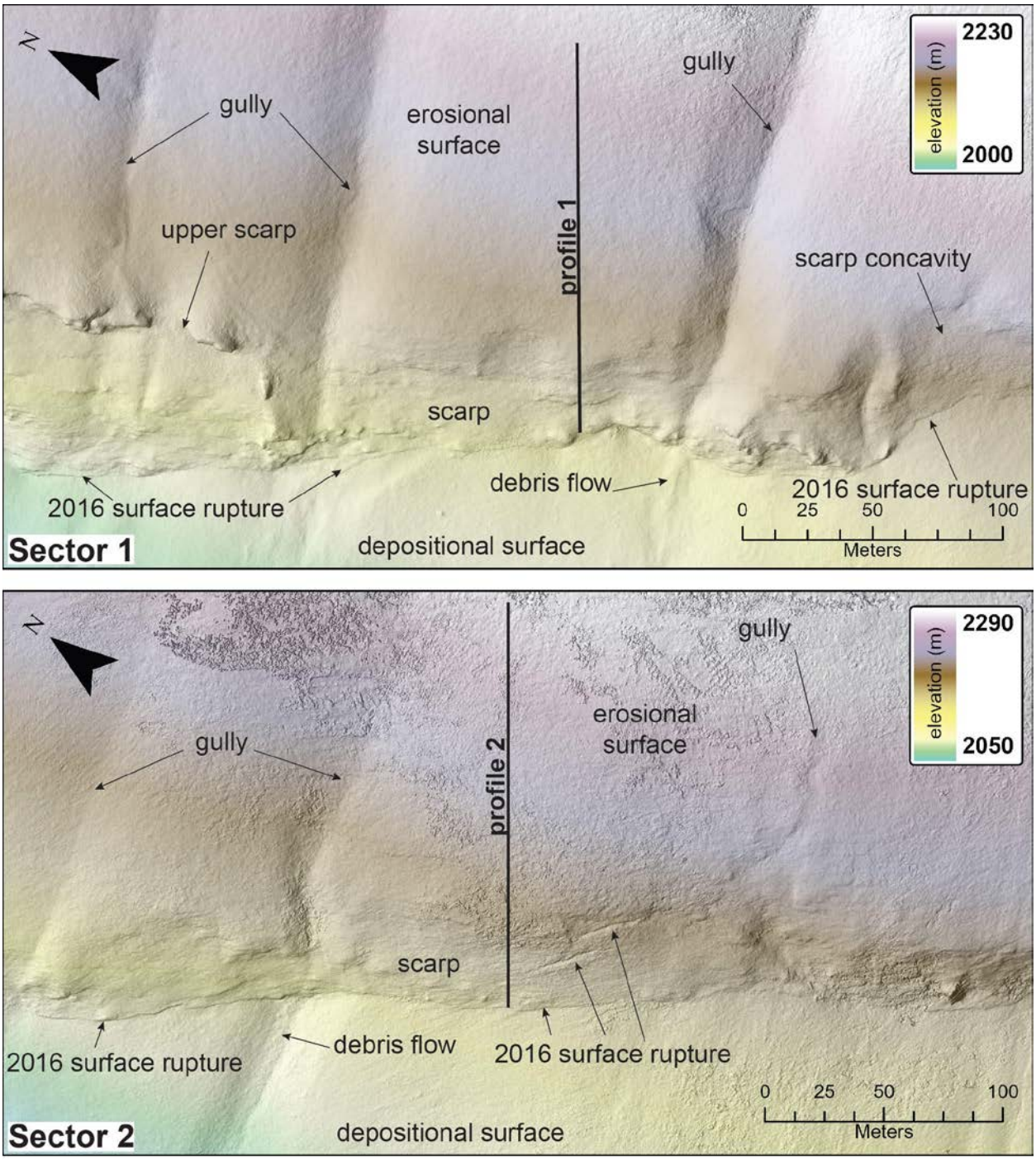

Figure 7. The main morphological features of the two sectors of the CDV fault scarp reconstructed by means of SfM-derived DSM. See figure 4 for location.

Figure 8 shows the spatial distribution of the slope angle with respect to elevation change (height from the scarp baseline) along the two sectors of the CDV fault scarp, which was useful to

pinpoint the scarp surface and the footwall erosional surface boundaries. The diagrams show that the slope angle changes along the surface, defining the areal extension and morphological characteristics of the CDV scarp and footwall erosional surface. Sector 1 presents a sharp slope change at the top of the scarp area: the footwall erosional surface displays an average slope of 33°, whereas the scarp area shows large patches of slope maxima ranging 75°-85°. In this sector, the scarp is composed of an upper part, ~10-15 m high, to the north-west, and a lower part, with elevation from baseline ranging from 50 to 40 m. Sector 2 presents a smoother slope change at the top of the scarp area: the footwall erosional surface displays an average slope of 35°, whereas the scarp area shows large patches of slope ranging 65°-70°. In this sector, the scarp has an elevation from baseline that reaches ~40 m.

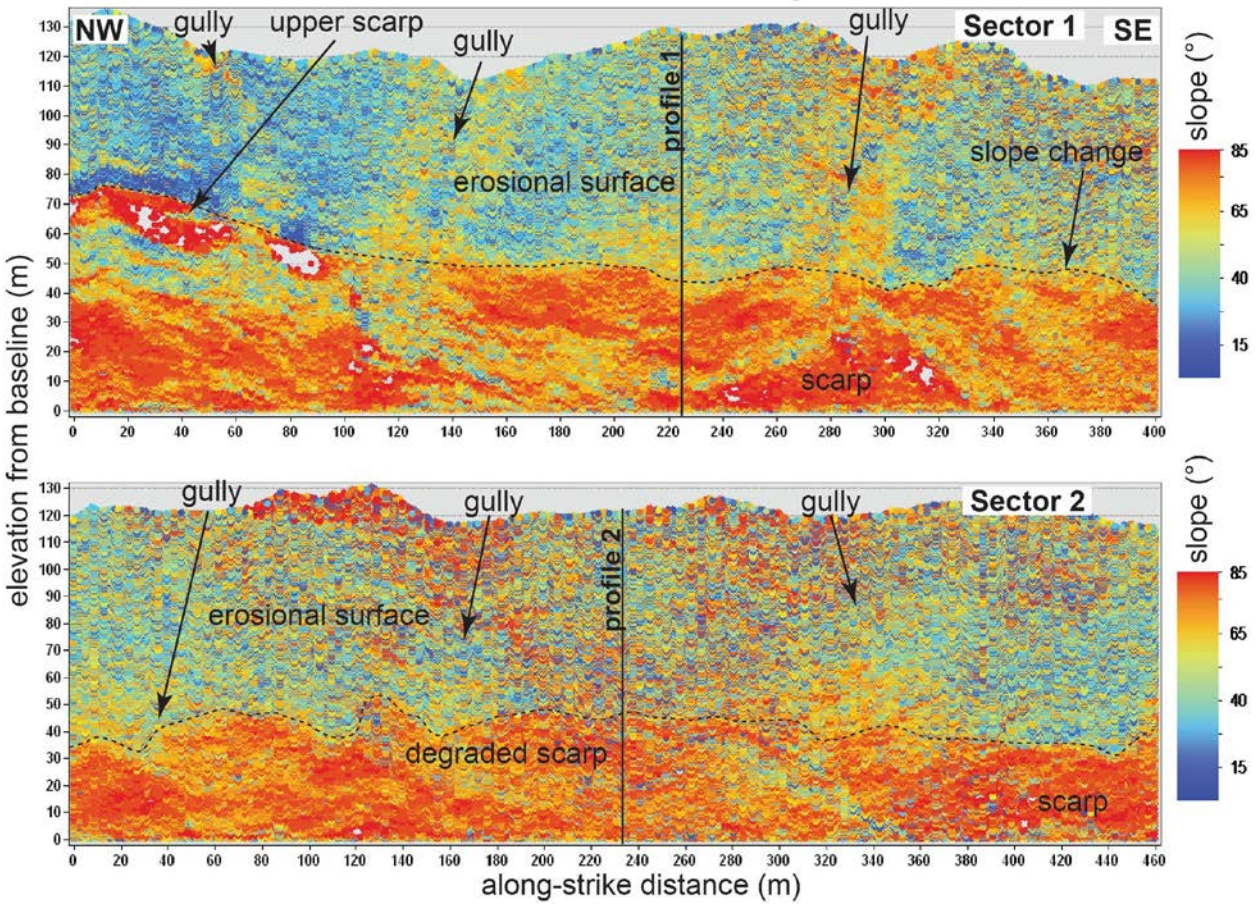

Figure 8. Diagram of the spatial distribution (elevation vs. along-strike distance) of the slope for the two sectors of the CDV fault scarp.

4.2 The long-term throw

From each profile, we get the long-term cumulative throw of the CDV fault by including the degraded upper part of the morphological scarp (i.e. eroded fault plane) using Eq. 1 (see ch. 3.3 and Fig. 9). From the regression line of the footwall erosional surface, we obtain the slope angle (γ) and the intercept coefficient (representing the surface offset S). The coefficients of determination (R^2) derived from all of the regression lines show an overall excellent fit with the sampled points (the lower fits are influenced by erosional gullies) (Fig. 9b). This justifies the assumption that the footwall erosional surface was a quasi-planar morphological marker. The intercept coefficient of each single profile presents low uncertainty (< 0.3 m). This translates into a throw formal error that is one order of magnitude smaller than the precision given by the statistical analysis of the whole along-strike distribution of the sampled throws (i.e. mode and confidence interval from the distribution of the most representative values of the CDV scarp; see following main text).

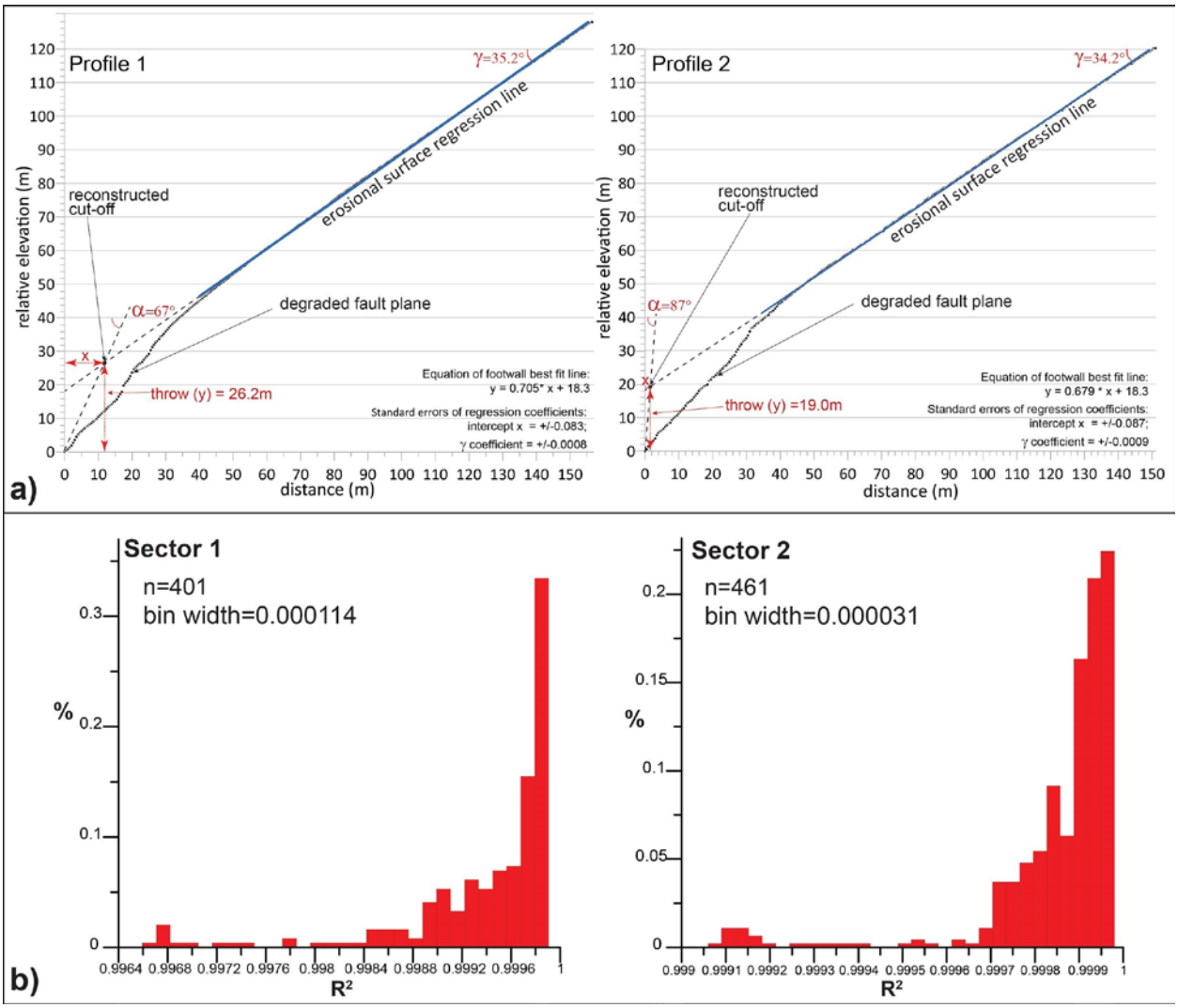

Figure 9. a) Illustrative topographic profiles extracted from the SfM-derived DSM at the two sectors (see Figs. 7 and 8 for location). The best fit line representing the erosional surface is reported along with the equation parameters. In red are reported the value of the input variables used to solve Eq. 1 for the throw estimate; **b)** Histograms showing the frequency distribution of the coefficient of determination (R^2) for the regression lines approximating the erosional surface at both sectors. Bin width calculated using the Freedman-Diaconis rule (Freedman and Diaconis, 1981).

The dip angle (α) of the fault plane data used in the calculation (Eq. 1, ch. 3.3) derive from the measurements of the bedrock slickensides, affected by the coseismic movement (i.e. exposure of a white ribbon of fresh limestone) during the 30th October 2016 earthquake surface faulting. It

shows a SW-plunging dip angle (α) ranging from 58° to 90° (Fig. 10a), with bimodal distribution around 71° and 77° and a strike clustered around N145°-150°, parallel to the morphological CDV scarp (Fig. 10b).

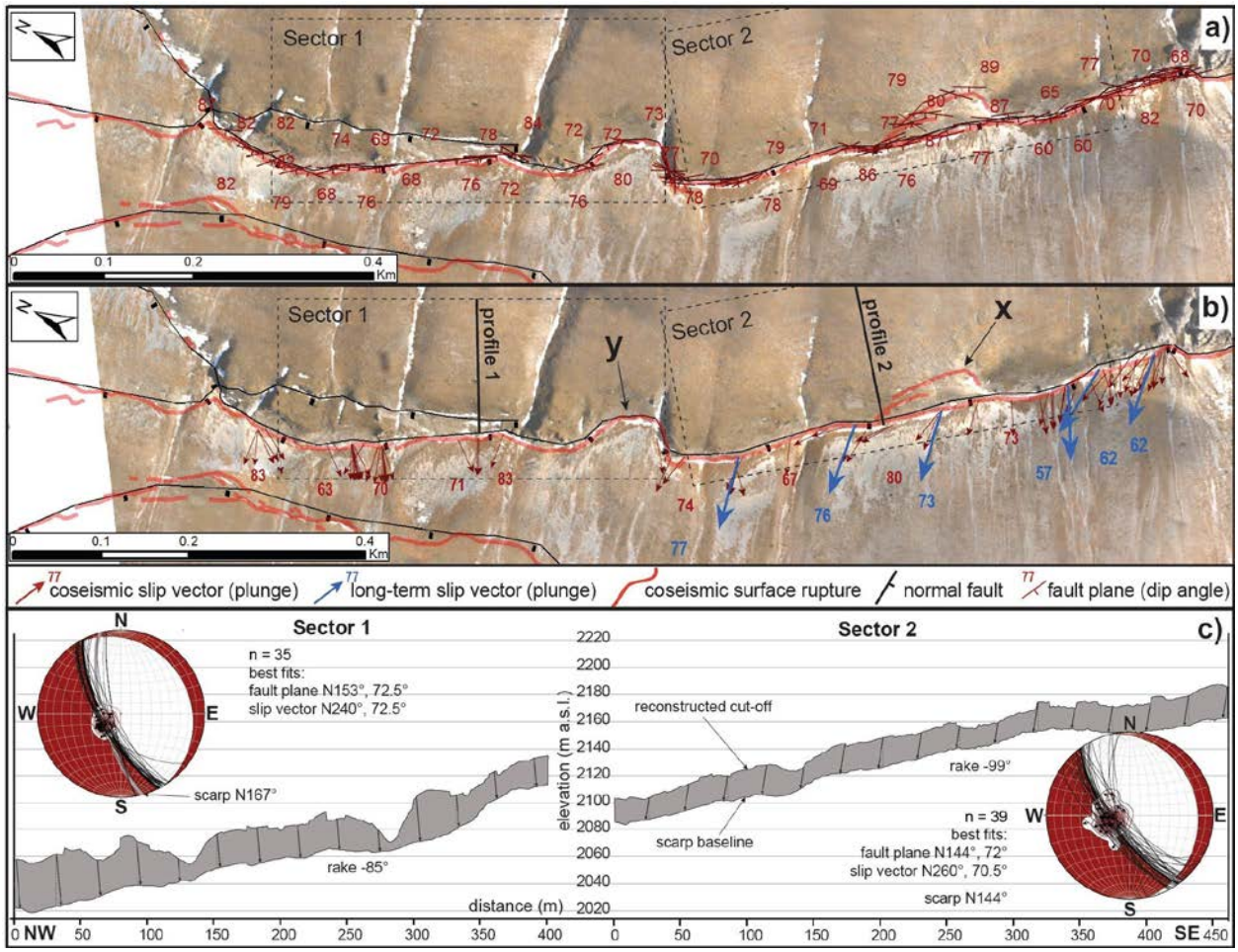

Figure 10. a) Detailed map of the CDV fault (black lines) with the 30th October 2016 coseismic surface ruptures (red lines). The DOPs of the CDV area is adopted as a basemap. The coseismic fault planes measured along the bedrock slickensides are reported with dip angles (red symbols and numbers); **b)** Both long-term CDV normal fault plane and 2016 coseismic slip vectors (blue and red arrows, respectively) measured along the bedrock slickensides are reported with plunges (blue and red numbers, respectively); **c)** Along-strike elevation profile of the reconstructed CDV fault scarp showing the 2016 coseismic rake (i.e. kinematics indicator on the fault plane, following notation of Aki and Richards, 1980) of the two sectors. For each sector the kinematic strain field is reported, represented as a focal mechanism from the statistical analysis of the 2016 coseismic fault planes (black semi-circles) and slip vectors (black arrows). The average strike of the CDV scarp (gray semi-circle) and best fit of fault planes (thick black semi-circle) and slip vectors (contouring) are also shown (Schmidt stereonet, lower hemisphere).

4.3 Spatial distribution of the CDV scarp throw

The diagram of the spatial distribution (along-strike distance) of the long-term CDV scarp throw reconstructed using Eq. 1 for each cross profile shows a variability mostly related to large minima due to the scarp dissection within gully incision areas (Fig. 11). In order to provide epistemic uncertainty estimates derived from α, we show two spatial distribution curves: 1) throw by means of Eq. 1, with dip angle (α) from field-measured fault planes (blue line in Fig. 11); and 2) surface offset from regression lines intercept, representing the minimum possible throw, with $\alpha = 90°$ (green line in Fig. 11). The DSM-derived scarp slope angle was not considered in the calculation since it largely deviates from the actual dip of the fault plane due to its considerable degradation that would yield unrealistic higher throw values (Fig. 5b and 5c).

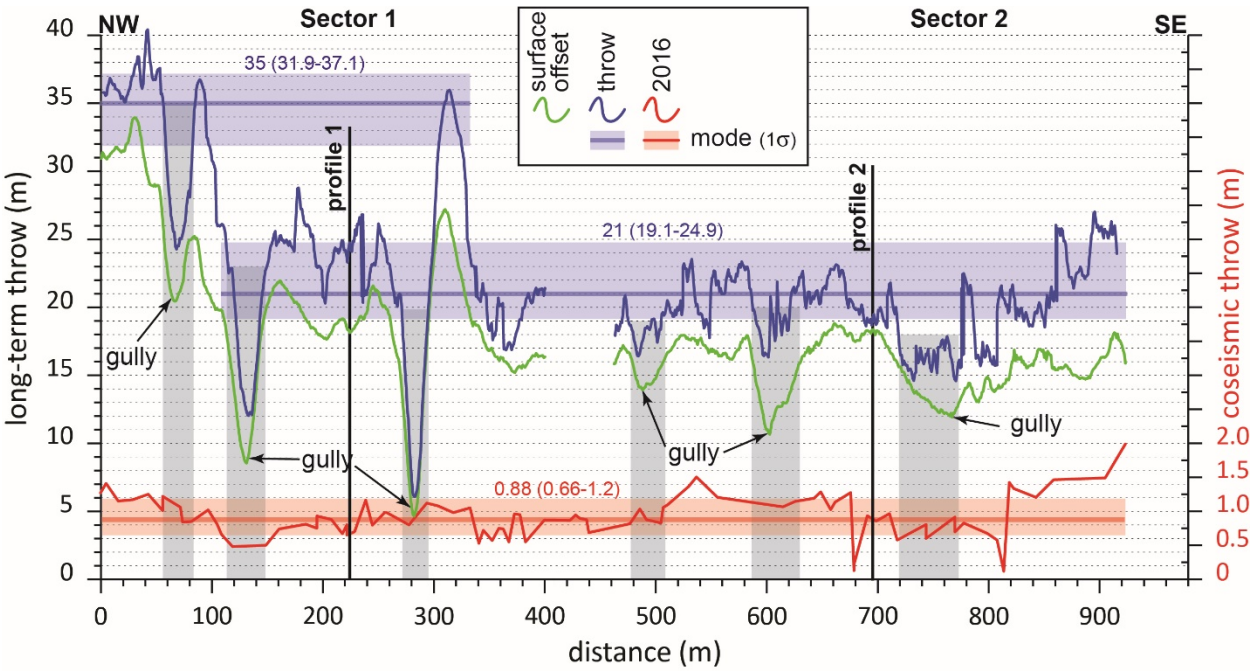

Figure 11. Diagram of the spatial distribution (along-strike distance) of the calculated CDV long-term and 2016 coseismic throws (blue and red lines, respectively), presented as raw data, mode and 1σ confidence interval (68.3%) of throws (see Fig. 12) for the two sectors. The mode and confidence interval of throw are split into the upper and main scarps, as suggested by the bimodal frequency distribution of the data shown in Figure 12. CDV surface offset curve (green line) is reported to show the minimum plausible throw. Grey vertical rectangles highlight the data of long-term throw affected by gully erosion and removed from the mode calculation. 2016 coseismic throws data are from Villani et al. (2018).

Sector 1 shows throws with a maximum peak of ~41 m at the northwestern edge (with ~34 m of surface offset). Sector 2 shows throws with a maximum of ~27 m (with ~19 m of surface offset) (Fig. 11). The bimodal frequency distribution of the calculated throws show two peaks with non-normal distribution around a mode of 21 m (1σ - 68.3% confidence interval - = 19.1-24.9 m) and 35 m (1σ = 31.9-37.1 m), with the latter representing the upper scarp of Sector 1 (Figs. 6a and 7). These values must be considered as a minimum, bearing in mind the conservative assumption made about the hangingwall erosional surface cut-off (see ch. 3.3).

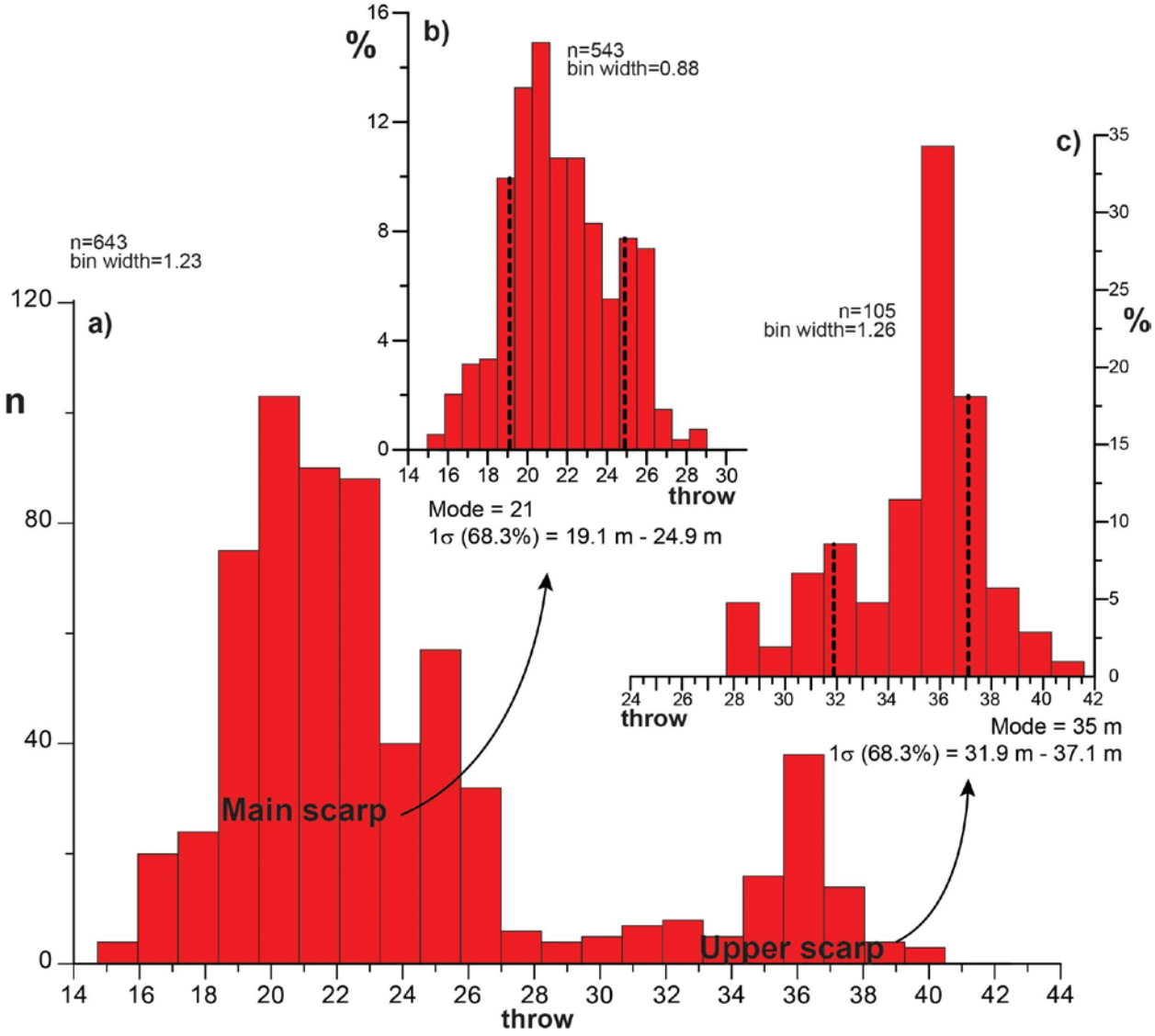

Figure 12. a) Histograms showing the bimodal frequency distribution of the whole CDV fault throw derived from Eq. 1), discarding data from gully incision areas (see Fig. 11). The histograms of the non-normal frequency distribution of the two peaks representing the main **(b)** and the upper **(c)** scarps are reported along with the mode and the 1σ (68.3%) confidence interval of the distributions (dashed black lines). Bin width from Freedman-Diaconis rule (Freedman and Diaconis, 1981).

5. Discussion

5.1 Comparing long-term and coseismic throws

The 2016 coseismic surface faulting runs at the base of the main long-term CDV scarp, where fault slickensides crop out, showing no reactivation of the Sector 1 upper scarp. The finite strain derived from the kinematic analysis of the 30th October 2016 coseismic surface ruptures measured along bedrock slickensides indicates an almost pure dip slip movement along a plane striking N149° and dipping 72° SW (Fig. 10b). These coseismic kinematics appears to be similar to that occurred in the past, as evidenced by the long-term slip vectors measured from fault plane indicators (striae and slickenlines).

The 2016 coseismic reactivation of the CDV fault with similar structural arrangement and kinematics as in the past, suggests that the long-term CDV morphologic scarp was built as a result of repeated surface faulting events. Moreover, the consistent dip-slip fault motion allows us to assume that the morphological elevation change represents the vertical component of the net geological slip along the CDV fault plane.

In this light, we performed a comparison between the long-term main CDV scarp and the 2016 coseismic surface faulting throws. Along the two studied sectors, the 2016 coseismic throw is not influenced by the substratum, appearing to disregard the different bodies of unconsolidated deposits and crosscutting debris cones fed by gullies. It presents a modal value of throw of 0.88 m (1σ = 0.66-1.2 m) (Fig. 11). The increase of the long-term throw values along Sector 1 of the CDV scarps does not match the trend of the 2016 coseismic rupture. This discrepancy could derive from: 1) the slip distribution that does not remain the same during the subsequent surface faulting events; 2) the LGM erosive process was spatially irregular in extent and efficiency and did not completely obliterate an earlier fault scarp morphology (e.g. the upper scarp of Sector 1, Fig. 11); 3) the post-

LGM weathering processes affecting the CDV fault scarp were spatially uneven in extent and efficiency and produced later inset erosional surfaces (e.g. the southeastern part of the scarp).

5.2 Insights into scarp age and tectonic rates

The homogeneity of the well-preserved bedrock erosional surface supports the hypothesis that the footwall of the main CDV scarp was affected by the same spatial and temporal distribution of the periglacial-glacial surface process and represents a LGM marker. Therefore, we can infer that the main CDV fault scarp results from the minimum cumulative offset following the LGM.

However, it is difficult to attribute an age to such LGM erosional markers by means of absolute dating methods. The exposure-age cosmogenic ^{36}Cl dating of the top surfaces of the LGM scarps is strongly influenced by even small erosion rates and requires estimating the snow cover through time (Gosse and Phillips, 2001; Balco et al., 2008). In the Apennines, this dating methodology was applied on a single fault scarp footwall, providing a minimum age coinciding with the demise of the LGM (Cowie et al., 2017).

The small Late Wurmian glaciers of the Mt. Sibillini range were active until 14-15 ka cal BP (Mount Aquila 1 Stade) and can be invoked as responsible for the erosional surface production. Their location was limited to an elevation of 1550-1900 m a.s.l. that progressively raised of more than 600 m (Giraudi 2004; Giraudi 2015) (Fig.13). According to these authors, the LGM is characterized by three main oscillations of alternating warmer climatic conditions and glaciers retreats: a first around 25-27 ka cal BP (post-Campo Imperatore Stade); a second major recessional phase between 18 and 21 ka cal BP (Cento Monti and Fornaca Interstades); a third recessional phase (Venaquaro Interstade) around 13-14 ka cal BP (Fig.13). To assign an age to the CDV

footwall erosional surface, we can correlate to the glacier retreat phases the throws calculated from the main and upper CDV scarps (Fig.13).

Considering that the equilibrium line altitude (ELA) calculated for the glaciers was confidently set below the CDV fault scarp elevation only during the first and second recessional phases (Giraudi, 2015), given also the southwestern exposure of the Mt. Vettore flank, the age of the LGM marker is more likely 25-27 ka cal BP or 18-21 ka cal BP. If this is the case, taking into account the first or second recessional phases as responsible for the generation of the footwall erosional surface, the throw of 21 m (1σ = 19.1-24.9 m) would imply a throw rate of 0.78-0.84 mm/a (1σ = 0.7-1.0 mm/a) or 1.0-1.17 mm/a (1σ = 0.91-1.38 mm/a), respectively (Fig.13). Such values are smaller than the estimate of 1.0-1.9 mm/a provided in the same area by Brozzetti et al. (2019) and Puliti et al. (2021) on the basis of the topographic displacement (measured along few profiles on a 2- to 5-m resolution DTMs) accumulated considering a younger post-LGM (set after 12-18 ka ago).

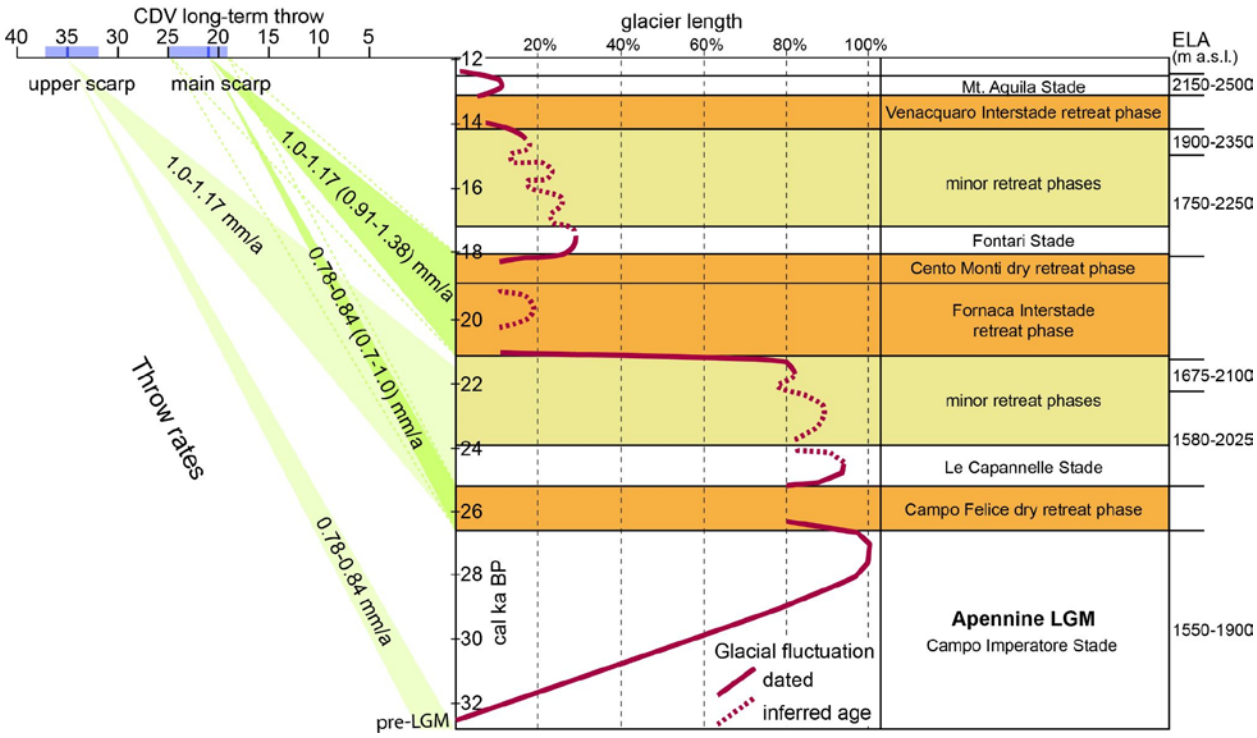

Figure 13. Chronology of the Apennines LGM and deglaciation phases according to Giraudi (2015). The correlation of the post-glacial long-term throws of the CDV with the retreat phases as reported indicating possible ages and throw-rates.

These throw rates are comparable with the estimates derived from the net stratigraphic throws, calculated by means of cross sections, that reach a maximum value of 470 m across the CDV fault scarp (Brozzetti et al., 2019) and 1400 m across the aggregate VBFS splays composing the Mt. Vettore fault system (Villani et al., 2019; Porreca et al., 2020). In fact, considering the age uncertainty of the onset of the extension in the study area (1.0-2.0 Ma; Cavinato and De Celles, 1999), the throw rates range between 0.7 and 1.4 mm/a for the entire VBFS. Assuming that the CDV fault is a younger splay of the VBFS that lately contributes to most of the throw rate, accommodating a net throw of 470 m, its onset would occur between ~400 ky and ~720 ky ago. Most of the data about the long-term throw rates of the Apennines faults (smoothing short-term slip clustering) show values below 1.0 mm/a (e.g. Roberts and Michetti, 2004; Faure Walker et

al., 2009; Cowie et al., 2017; Cinti et al., 2019). In the hypothesis of no inherited pre-orogenic extensional slip, the lower range of our throw rate estimates appears more likely: CDV fault age of ~720 ka, with a scarp age of 25-27 ka and throw-rate of 0.78-0.84 mm/a (1σ = 0.7-1.0 mm/a).

These results suggest that the Apennines glaciation- and periglacial-related regional markers can be correlated with different post-LGM (or even pre-LGM) major glacial retreat phases, providing throw rate estimates that reconcile with the generally slower long-term values. Moreover, they suggest that the erosional processes acting up to the pre-Fornaca Interstade, regardless of their specific nature and location, could not provide a unique regional marker by erasing any pre-existing neo-forming bedrock fault scarp. Furthermore, in literature we note an overestimation of the throw rates due to the misuse of uncalibrated radiocarbon age of the major Fornaca Interstade post-LGM marker (~16–18 ka ^{14}C) instead of calibrated calendar ages (~19-21 ka cal BP).

Moreover, following our analysis, in this sector of the Apennines, the upper range of the extensional phase onset (2.0 Ma; Cavinato and De Celles, 1999) is more reliable and agrees with the up to 550-m thick Quaternary infill of the fault-controlled Castelluccio Basin (Sapia et al., 2021), although caution should be paid due to the lack of chronological constraints on the age of the subsurface sediments.

5.3 Speculations on the CDV fault earthquake recurrence time

With the assumption that the average coseismic throw distribution along the CDV was the same during successive surface faulting earthquakes, by using the 2016 throw as a reference, we can calculate that the present CDV formed via accumulation of ~24 (1σ = ~16-38) 2016-type ruptures.

If these events occurred in the past 25-27 ka or 18-21 ka, we can infer an average recurrence time interval of ~1,040-1,125 (1σ = ~660-1,690) or ~750-875 (1σ = ~470-1,310) years, respectively. These values are shorter with respect to the average recurrence time obtained from paleoseismological studies along the VBFS that are 3,360–3,640 years for the past ~22 ka and 1,220–1,970 years for the past ~4 ka (Cinti et al., 2019). However, this paleoseismological record derives from secondary ruptures that may activate only during the largest events and, as common, may have missed some old paleoseismic event. Regardless of such uncertainties, the ~1,100 years earthquake recurrence obtained from this work : 1) can be taken as the most plausible, if the recurrence time interval for the past ~4 ka deriving from paleoseismology is representative of the previous millennia and does not represent an acceleration of the seismic activity of the VBFS; 2) indicates that the CDV scarp age was underestimated (being possibly pre-LGM), if the longer recurrence time interval for the past ~22 ka deriving from paleoseismology is truly representative for the VBFS. In summary, the CDV scarp age is not younger than 25-27 ka, as assumed for the throw rate estimate.

5.4 Competition between erosive and tectonic processes at the CDV scarp

Notably, the long-term throw presents minima in coincidence with the scarp incisions produced by the gullies. Such incisions counteract the scarp growth and testify the local efficiency of the down-cutting process. In this regard, the along-strike throw distribution provides an opportunity to inform on the incision rates that counteract the fault scarp growth where the drainage crosses the CDV scarp. In Sector 1, given the calculated throw of 21 m (1σ = 19.1-24.9 m), the up to 15 m (1σ = 13.1-18.9 m) incision height (from the deepest gully of Sector 1, Fig. 11) suggests an incision rate of 0.56-0.6 mm/a (1σ = 0.52-0.69 m) for the last 25-27 ka. This rate

should be considered as a minimum, because the age of the gully inception could be much younger than the scarp age. In general, the CDV scarp displays incision and throw rates of the same order of magnitude, evidencing the efficacy of such surface processes in competing with tectonics.

Along the CDV fault scarp, we did not clearly recognized sub-horizontal bands of different grades of weathering, as those originated from fault surface exposed in subsequent times due to repeated slip events (karstification, bioerosion, and weathering; e.g., Carcaillet et al., 2008; Giaccio et al., 2003; Wiatr et al., 2015). This is probably because the long-term action of the degradational processes affecting the scarp slope occur with irregular distribution so as to smooth the weathering bands. As part of the degradational processes affecting the scarp, it is worth noting the 2016 coseismic downdip concave upper splay along Sector 2, with no long-term escarpment (indicated with x in Fig. 10b). It represents an incipient shallow gravitational detachment of the morphologic scarp that, in the future, could produce a concave interruption of the CDV scarp linearity similar to that visible at the southeastern edge of Sector 1 (y in Fig. 10b). This suggests the possible occurrence of rock avalanches as further surface process of fault scarp evolution.

6. Conclusions

We reconstructed a significant portion of the long-term CDV bedrock fault scarp, and a periglacial-glacial erosional landform at its footwall through a 0.15 m/pixel resolution SfM-derived DSM of the western flank of Mt. Vettore. The CDV was the locus of Mw 6.0 and 6.5 2016 earthquakes coseismic ruptures, and the comparison between long-term and coseismic throws enabled us to use it as a geomorphic marker for throw and throw rates calculations. We propose a method that allows us to retrieve a minimum long-term throw from a tectonic scarp also where offset geomorphologic markers are buried at the fault hangingwall. This is done by means of a

series of closely spaced cross-profiles, from both field and DSM data, and solving the equations of the two non-parallel lines describing the footwall erosional surface and the fault plane, taking into account the degraded part of the scarp and the fault kinematics.

We provided the along-strike distribution curve of the long-term CDV compound scarp throw resulting in a minimum modal throw value of ~35 and ~21 m for the upper and main scarps, respectively.

In order to get a maximum, plausible Late Pleistocene throw rate of the CDV fault (~0.8 mm/a, comparable with those of other Apennines faults), we suggest a minimum age of 25-27 ka cal BP for the main CDV scarp throw, by correlation of the erosional surface with the updated chronology of the Apennines LGM and deglaciation phases (Giraudi, 2015).

These results suggest that the Apennines glaciation- and periglacial-related regional markers can be correlated with different post-LGM (or even older than LGM) major glacial retreat phases, much older than the 12-18 ka BP generally used to get throw rates of the Apennines normal faults. In general, we are aware that the erosional processes could not provide a unique regional marker by erasing any pre-existing neo-forming bedrock fault scarp.

Assuming constant displacement per event at the site, we also suggest that ~24 repeated, 30th October 2016-type surface faulting events, are required to generate the present surface offset and long-term throw along the CDV fault in the past 25-27 ka. This also provides an average recurrence interval for 30th October 2016-type events of ~1100 years, in agreement with that inferred from paleoseismological data collected in the area for the past ~4 ka (Cinti et al., 2019).

Besides the specific results on the CDV scarp that enrich our knowledge on the VBFS, this work provides an affordable workflow for tectonic scarp geomorphological analysis and for fault zone topography mapping in areas of sparse or low-lying vegetation. This is an example of SfM

application showing how it greatly facilitates the imaging of subtle geomorphic offsets related to faulted landscapes.

Acknowledgements

This work was funded by INGV (salaries) and benefited of the activities carried out in the framework of the EMERGEO Working Group during the 2016-2017 Central Italy earthquake sequence that were funded by an agreement between the Istituto Nazionale di Geofisica e Vulcanologia and the Italian Civil Protection Department (DPC-INGV 2012-2021, Allegato A). The Pleiades images were provided by the CEOS Seismic Hazards Pilot from ESA and the ISIS program from CNES, France. Constructive comments and suggestions provided by three anonymous reviewers definitely helped in improving the final version of the manuscript.

Data Availability

The high-resolution digital surface model (DSM) of the CDV fault scarp reconstructed by means of the 3D photo-based 'Structure-from-Motion' (SfM) technique and the dataset of oblique aerial photographs (raw image files *.arw and *.nef) related to this article can be found at the INGV Repository MoDiSMoL "Rilievi fotogrammetrici digitali e ricostruzioni modelli tridimensionali mediante tecnica Structure-from-Motion (SfM) and Lidar" (ID 271, Class 10, Level 2). URL is provided on request by the authors Stefano Pucci or Riccardo Civico (riccardo.civico@ingv.it; stefano.pucci@ingv.it). Structural data used in this work are available on request to the contact Author, while all the coseismic data are contained in the database of coseismic effects following the 2016 Norcia earthquake: Villani, F. et al. PANGAEA https://doi.org/10.1594/PANGAEA.879469 (2017).

References

Allen R. M., Nolet G., Morgan W. J., Vogfjörd K., Bergsson B. H., Erlendsson P. Foulger G. R., Jakobsdóttir S., Julian B. R., Pritchard M., Ragnarsson S., Stefánsson R. (1999). The thin hot plume beneath Iceland. *Geophys. J. Int.*, 137, 51–63. doi: 10.1046/j.1365-246x.1999.00753.x

Allmendinger R. W., Cardozo N., Fisher D. (2012). *Structural geology algorithms: Vectors and tensors in structural geology*. Cambridge, UK: Cambridge University Press. pp. 302.

Armijo R., Tapponnier P., Mercier J. L., Han T. L. (1986). Quaternary extension in southern Tibet: Field observations and tectonic implications. *Journal of Geophysical Research: Solid Earth*, 91 (B14), 13803-13872. doi: 10.1029/JB091iB14p13803

Armijo R., Lyon-Caen H., Papanastassiou D. (1992). East-west extension and Holocene normal-fault scarps in the Hellenic arc. *Geology*, 20 (6), 491-494. doi: 10.1130/0091-7613(1992)020<0491:EWEAHN>2.3.CO;2

Balco G., Stone J. O., Lifton N. A., Dunai T. J. (2008). A complete and easily accessible means of calculating surface exposure ages or erosion rates from 10Be and 26Al measurements. *Quaternary geochronology*, *3* (3), 174-195.

Barchi M., Galadini F., Lavecchia G., Messina P., Michetti A. M., Peruzza L., Pizzi A., Tondi E., Vittori E. (2000). *Sintesi delle conoscenze sulle faglie attive in Italia Centrale: Parametrizzazione ai fini della caratterizzazione della pericolosità sismica*. GNDT, Gruppo Nazionale per la Difesa dai Terremoti, Roma, spec, publ., 62 pp.

Basili R., Bosi V., Galadini F., Galli P., Meghraoui M., Messina P., Moro M., Sposato A. (1998). The Colfiorito earthquake sequence of September–October 1997: surface breaks and seismotectonic implications for the central Apennines (Italy). *Journal of Earthquake Engineering*, 2 (2), 291-302.

Benedetti L., Finkel R., Papanastassiou D., King G., Armijo R., Ryerson F., Farber D., Flerit F. (2002). Post-glacial slip history of the Sparta fault (Greece) determined by 36Cl cosmogenic dating: Evidence for non-periodic earthquakes. *Geophys. Res. Lett.*, 29 (8), doi: 10.1029/2001GL014510.

Benedetti L., Finkel R., King G., Armijo R., Papanastassiou D., Ryerson F. J., Flerit F., Farber D.,

Stavrakakis G. (2003). Motion of the Kaparelli fault (Greece) prior to the 1981 earthquake sequence determined from 36Cl cosmogenic dating. *Terra Nova*, 15 (2), 118–124.

Benedetti L., Manighetti I., Gaudemer Y., Finkel R., Malavieille J., Pou K., Arnold M., Aumaitre G., Bourles D., Keddadouche K. (2013). Earthquake synchrony and clustering on Fucino faults (Central Italy) as revealed from in situ 36Cl exposure dating. *Journal of Geophysical Research: Solid Earth*, 118, 4948–4974. doi: 10.1002/jgrb.50299.

Bemis S. P., Micklethwaite S., Turner D., James M. R., Akciz S., Thiele S. T., Bangash H. A. (2014). Ground-based and UAV-based photogrammetry: A multi-scale, high-resolution mapping tool for structural geology and paleoseismology. *Journal of Structural Geology*, 69, 163-178. doi: 10.1016/j.jsg.2014.10.007

Blumetti A. M., Guerrieri L. (2007). Fault-generated mountain fronts and the identification of fault segments: implications for seismic hazard assessment. *Bollettino Società Geologica Italiana*, 126 (2), 307.

Blumetti A. M., Dramis F., Michetti A. M. (1993). Fault-generated mountain fronts in the central Apennines (Central Italy): Geomorphological features and seismotectonic implications. *Earth Surface Processes and Landforms*, 18 (3), 203-223. doi: /10.1002/esp.3290180304

Blumetti A. M. (1995). Neotectonic investigations and evidence of paleoseismicity in the epicentral area of the January-February 1703, central Italy, earthquakes: In: Serva L. & Slemmons B. Eds., Perspectives in Paleoseismology. *Ass. of Engineering Geologists, Spec. Publ.*, 6, 83-100.

Boncio P., Lavecchia G., Pace B. (2004). Defining a model of 3D seismogenic sources for seismic hazard assessment applications: The case of central Apennines (Italy). *Journal of Seismology*, 8, 408–425.

Boncio P., Pizzi A., Brozzetti F., Pomposo G., Lavecchia G., Di Naccio D., Ferrarini F. (2010). Coseismic ground deformation of the 6 April 2009 L'Aquila earthquake (central Italy, Mw6. 3). *Geophysical Research Letters*, 37 (6). doi: 10.1029/2010GL042807.

Bosi C. (1975). Osservazioni preliminari su faglie probabilmente attive nell'Appennino Centrale. *Boll. Soc. Geol. It.*, 94, 827-859.

Bosi C., Galadini F., Giaccio B., Messina P., Sposato A. (2003). Plio-Quaternary continental deposits

in the Latium-Abruzzi Apennines: the correlation of geological events across different intermontane basins. *Il Quaternario*, 16 (1 Bis), 55-76.

Brozzetti F., Boncio P., Cirillo D., Ferrarini F., de Nardis R., Testa A., Liberi F., Lavecchia G. (2019). High-resolution field mapping and analysis of the August–October 2016 coseismic surface faulting (central Italy earthquakes): Slip distribution, parameterization, and comparison with global earthquakes. *Tectonics*, 38 (2), 417-439. doi: 10.1029/2018TC005305

Brunori C. A., Civico R., Cinti F. R., Ventura G. (2012). Characterization of active fault scarps from LiDAR data: a case study from Central Apennines (Italy). *International Journal of Geographical Information Science*, 27 (7), 1405-1416. doi: 10.1080/13658816.2012.684385.

Bucknam, R. C., Anderson, R. E. (1979). Estimation of fault-scarp ages from a scarp-height–slope-angle relationship. *Geology*, 7 (1), 11-14.

Byrd J. O. D., Smith R. B., Geissman J. W. (1994). The Teton fault, Wyoming: Topographic signature, neotectonics, and mechanisms of deformation, *J. Geophys. Res.*, 99, 20,095–20,122.

Calamita F., Pizzi, A. (1992). Tettonica quaternaria nella dorsale appenninica umbro-marchigiana e bacini intrappenninici associati. *Studi Geologici Camerti*, 1992 (1), 17–25.

Calamita F., Pizzi A., Roscioni, M. (1992). I fasci di faglie recenti ed attive di M. Vettore – M. Bove e di M. Castello – M. Cardosa (appennino Umbro-Marchigiano). *Studi Geologici Camerti*, 1992 (1), 81–95.

Calamita F., Pizzi A. (1994). Recent and active extensional tectonics in the southern Umbro-Marchean Apennines (central Italy). *Memorie della Società Geologica Italiana*, 48, 541–548.

Carcaillet J., Manighetti I., Chauvel C., Schlagenhauf A., Nicole J. M. (2008). Identifying past earthquakes on an active normal fault (Magnola, Italy) from the chemical analysis of its exhumed carbonate fault plane. *Earth and Planetary Science Letters*, 271 (1-4), 145-158. doi: 10.1016/j.epsl.2008.03.059.

Carminati E., Doglioni C. (2012). Alps vs. Apennines: the paradigm of a tectonically asymmetric. Earth. *Earth-Science Reviews*, 112 (1-2), 67-96. doi: 10.1016/j.earscirev.2012.02.004.

Carson, M. A., and M. J. Kirkby (1972). Hillslope Form and Processes. Cambridge Univ. Press, New York, 476 pp.

Cavinato G. P., De Celles P. G. (1999). Extensional basins in the tectonically bimodal central Apennines fold-thrust belt, Italy: Response to corner flow above a subducting slab in retrograde motion. *Geology*, 27 (10), 955–958. doi: 10.1130/0091-7613(1999)027<0955: EBITTB>2.3.CO;2.

Cello G., Mazzoli S., Tondi E., Turco E. (1997). Active tectonics in the central Apennines and possible implications for seismic hazard analysis in peninsular Italy. *Tectonophysics*, 272 (1), 43–68. doi: 10.1016/S0040-1951(96)00275-2.

Cello G., Gambini R., Mazzoli S., Read A., Tondi E., Zucconi V. (2000). Fault zone characteristics and scaling properties of the Val d'Agri Fault System (Southern Apennines, Italy). *Journal of Geodynamics*, 29 (3-5), 293-307. doi: 10.1016/S0264-3707(99)00043-5

Centamore E., Adamoli L., Berti D., Bigi S., Casnedi R., Cantalamessa G., et al. (1992). *Carta geologica dei bacini della Laga e del Cellino e dei rilievi carbonatici circostanti (Marche meridionali, Lazio nord-orientale, Abruzzo settentrionale)*. Scale 1:100,000. Firenze, SELCA.

Chiarabba C., Chiodini, G. (2013). Continental delamination and mantle dynamics drive topography, extension and fluid discharge in the Apennines. *Geology*, 41 (6), 715–718. doi: 10.1130/G33992.1.

Chiarabba C., Jovane L., Di Stefano, R. (2005). A new view of Italian seismicity using 20 years of instrumental recordings. *Tectonophysics*, 305, 251–268. doi: 10.1016/j.tecto.2004.09.013.

Chiaraluce L., Di Stefano R., Tinti E., Scognamiglio L., Michele M., Casarotti E., Cattaneo M, De Gori P., Chiarabba C., Monachesi G., Lombardi A.M., Valoroso L., Latorre D., Marzorati S. (2017). The 2016 central Italy seismic sequence: A first look at the mainshocks, aftershocks and source models. *Seismological Research Letters*, 88 (3), 757–771. doi: 10.1785/0220160221.

Cinti F. R., Cucci L., Marra F., Montone, P. (1999). The 1997 Umbria-Marche (Italy) earthquake sequence: Relationship between ground deformation and seismogenic structure. *Geophysical Research Letters*, 26 (7), 895–898. doi: 10.1029/1999GL900142.

Cinti F. R., De Martini P. M., Pantosti D., Baize S., Smedile A., Villani F., Civico R., Pucci S., Lombardi A. M., Sapia V., Pizzimenti L., Caciagli M., Brunori C. A. (2019). 22-kyr-Long Record of Surface Faulting Along the Source of the 30 October 2016 Earthquake (Central Apennines, Italy), From Integrated Paleoseismic Data Sets. *Journal of Geophysical Research: Solid Earth*, 124 (8), 9021-9048. doi: 10.1029/2019JB017757.

Civico R., Pucci S., Villani F., Pizzimenti L., De Martini P. M., Nappi R., & the Open EMERGEO Working Group (2018). Surface ruptures following the 30 October 2016 Mw 6.5 Norcia earthquake, central Italy. *Journal of Maps*, 14 (2), 151–160. doi: 10.1080/17445647.2018.1441756.

Cowie P. A., Roberts G. P. (2001). Constraining slip rates and spacings for active normal faults. Journal of Structural Geology, 23 (12), 1901–1915. doi: 10.1016/S0191-8141(01)00036-0.

Cowie P. A., Phillips R. J., Roberts G. P., McCaffrey K., Zijerveld L. J. J., Gregory, L. C., Faure Walker J., Wedmore L. N. J., Dunai T. J., Binnie S. A., Freeman S. P. H. T., Wilcken K., Shanks R. P., Huismans R. S., Papanikolaou I., Michetti A. M., Wilkinson M. (2017). Orogen-scale uplift in the central Italian Apennines drives episodic behaviour of earthquake faults. *Scientific reports*, 7, 44858.

Delorme A., Grandi R., Klinger Y., Pierrot Deseilligny M., Feuillet N., Jacques E., Rupnik E., Morishita Y. (2020). Complex deformation at shallow depth during the 30 October 2016 Mw6. 5 Norcia earthquake: interference between tectonic and gravity processes? *Tectonics*, 39 (2), e2019TC005596.

DePolo C. M., Anderson J. G. (2000). Estimating the slip rates of normal faults in the Great Basin, USA. *Basin Research*, 12 (3-4), 227-240. doi: 10.1111/j.1365-2117.2000.00131.x.

DuRoss, C. B., Personius, S. F., Crone, A. J., Olig, S. S., Hylland, M. D., Lund, W. R., Schwartz, D. P. (2016). Fault segmentation: New concepts from the Wasatch fault zone, Utah, USA. *Journal of Geophysical Research: Solid Earth*, 121 (2), 1131-1157.

DuRoss C. B., Michael P. Bunds, Gold R. D., Briggs R. W., Reitman N. G., Personius S. F., Toké N. A. (2019). Variable normal-fault rupture behavior, northern Lost River fault zone, Idaho, USA. *Geosphere*, 15 (6), 1869–1892. doi: 10.1130/GES02096.1.

D'Agostino N., Jackson J. A., Dramis F., Funiciello R. (2001). Interactions between mantle upwelling, drainage evolution and active normal faulting: an example from the central

Apennines (Italy). *Geophysical Journal International*, 147 (2), 475–497. doi: 10.1046/j.1365-246X.2001.00539.x.

D'Agostino N., Avallone A., Cheloni D., D'Anastasio E., Mantenuto, S. (2008). Active tectonics of the Adriatic region form GPS and earthquake slip vectors. *Journal of Geophysical Research*, 113, B12413. doi: 10.1029/2008JB005860.

D'Agostino, N. (2014). Complete seismic release of tectonic strain and earthquake recurrence in the Apennines (Italy). *Geophysical Research Letters*, 41 (4), 1155-1162.

D'Anastasio E., De Martini P.M., Selvaggi G., Pantosti D., Marchioni A., Maseroli R. (2006). Short-term vertical velocity field in the Apennines (Italy) revealed by geodetic levelling data, *Tectonophysics*, *418* (3-4), 219-234, doi: 10.1016/j.tecto.2006.02.008.

EMERGEO Working Group (2010). Evidence for surface rupture associated with the MW 6.3 L'Aquila earthquake sequence of April 2009 (central Italy). *Terra Nova*, 22 (1), 43–51. doi: 10.1111/j.1365-3121.2009.00915.x.

EMERGEO Working Group (2016). Coseismic effects of the 2016 Amatrice seismic sequence: First geological results. *Annals of Geophysics*, 59 (5), 1–8. doi: 10.4401/AG-7195.

EMERGEO Working Group (2017). A new photographic dataset of the coseismic geological effects originated by the Mw 5.9 Visso and Mw 6.5 Norcia earthquakes (26th and 30th October 2016, Central Italy). *Miscellanea INGV*, 38, 1–114. http://www.ingv.it/editoria/miscellanea/2017/miscellanea34/.

Faure Walker J. P., Roberts G. P., Cowie P. A., Papanikolaou I. D., Sammonds P. R., Michetti A. M., Phillips, R. J. (2009). Horizontal strain-rates and throw-rates across breached relay zones, central Italy: Implications for the preservation of throw deficits at points of normal fault linkage. *Journal of Structural Geology*, 31 (10), 1145-1160. doi:10.1016/j.jsg.2009.06.011.

Faure Walker J. P., Roberts G. P., Sammonds P. R., Cowie P. (2010). Comparison of earthquake strains over 10^2 and 10^4 year timescales: Insights into variability in the seismic cycle in the central Apennines, Italy. *Journal of Geophysical Research: Solid Earth*, 115 (B10). doi: 10.1029/2009JB006462.

Faure Walker, J. F., Roberts, G. P., Cowie, P. A., Papanikolaou, I., Michetti, A. M., Sammonds, P.,

Wilkinson, M., McCaffrey, K.J.W., Phillips, R. J. (2012). Relationship between topography, rates of extension and mantle dynamics in the actively-extending Italian Apennines. *Earth and Planetary Science Letters*, 325, 76-84.

Fonstad M. A., Dietrich, J. T., Courville B. C., Jensen J. L., Carbonneau P. E. (2013). Topographic structure from motion: a new development in photogrammetric measurement. *Earth surface processes and Landforms*, 38 (4), 421-430. doi: 10.1002/esp.3366.

Frankel K. L., Dolan J. F., Finkel R. C., Owen L. A., Hoeft J. S. (2007). Spatial variations in slip rate along the Death Valley-Fish Lake Valley fault system determined from LiDAR topographic data and cosmogenic 10Be geochronology. *Geophysical Research Letters*, 34(18). doi: 10.1029/2007GL030549.

Frankel K. L., Owen L. A., Dolan J. F., Knott J. R., Lifton Z. M., Finkel R. C., Wasklewicz T. (2016). Timing and rates of Holocene normal faulting along the Black Mountains fault zone, Death Valley, USA. *Lithosphere*, 8 (1), 3–22. doi: 10.1130/L464.1.

Freedman D., Diaconis, P. (1981). On the histogram as a density estimator: L 2 theory. *Zeitschrift für Wahrscheinlichkeitstheorie und verwandte Gebiete*, *57* (4), 453-476.

Friedrich A. M., Wernicke B. P., Niemi N. A., Bennett R. A., Davis J. L. (2003). Comparison of geodetic and geologic data from the Wasatch region, Utah, and implications for the spectral character of Earth deformation at periods of 10 to 10 million years. *Journal of Geophysical Research: Solid Earth*, 108 (B4), 2199, doi: 10.1029/2001JB000682.

Galadini F., Galli P. (1999). The Holocene paleoearthquakes on the 1915 Avezzano earthquake faults (central Italy): Implications for active tectonics in the central Apennines. *Tectonophysics*, 308 (1-2), 143–170. doi: 10.1016/S0040-1951(99)00091-8.

Galadini F., Galli P. (2000). Active tectonics in the central Apennines (Italy)- Input data for seismic hazard assessment. Natural Hazards, 22 (3), 225–268. doi: 10.1023/A:1008149531980.

Galadini F., Galli P. (2003). Paleoseismology of silent faults in the central Apennines (Italy): The Mt. Vettore and Laga Mts. Faults. *Annals of Geophysics*, 46 (5), 815–836.

Galli P., Galadini F., Calzoni F. (2005). Surface faulting in norcia (central italy): A "paleoseismological perspective". *Tectonophysics*, 403 (1-4), 117-130. doi:10.1016/j.tecto.2005.04.003.

Galli P., Galadini F., Pantosti D. (2008). Twenty years of paleoseismology in Italy. *Earth-Science Rev.*, 88, 89–117. doi:10.1016/j.earscirev.2008.01.00.

Galli P., Galderisi A., Peronace E., Giaccio B., Hajdas I., Messina P., Pileggi D., Polpetta F. (2019). The awakening of the dormant Mount Vettore fault (2016 central Italy earthquake, Mw 6.6): Paleoseismic clues on its millennial silences. *Tectonics*, 38 (2), 687-705. doi.org/10.1029/2018TC005326.

Gallup, D., Frahm, J. M., Mordohai, P., Yang, Q., Pollefeys, M. (2007). Real-time plane-sweeping stereo with multiple sweeping directions. In *2007 IEEE Conference on Computer Vision and Pattern Recognition*, 1-8, IEEE.

Giaccio B., Galadini F., Sposato A., Messina P, Moro M., Zreda M., Cittadini A. (2003). Image processing and roughness analysis of exposed bedrock fault planes as a tool for paleoseismological analysis: results from the Campo Felice fault (central Apennines, Italy). *Geomorphology*, 49 (3-4), 281-30. doi: 10.1016/S0169-555X(02)00191-5.

Giraudi, C. (1995). Considerations on the significance of some post-glacial fault scarps in the Abruzzo Apennines (Central Italy), *Quat. Int.*, 25, 33–45.

Giraudi, C. (2004). The Apennine glaciations in Italy. Quarternary glaciations–extent and chronology, part I: Europe. *Developments in quaternary science*, 2, 215-224.

Giraudi, C. (2015). The upper Pleistocene deglaciation on the Apennines (peninsular Italy). *Cuadernos de investigación geográfica*, 41 (2), 337-358. doi: 10.18172/cig.2696.

Giraudi C., Frezzotti, M. (1997). Late Pleistocene glacial events in the central Apennines, Italy. *Quaternary Research*, 48 (3), 280-290. doi: 10.1006/qres.1997.1928P.

Ghisetti F., Vezzani, L. (1999). Depth and modes of Pliocene–Pleistocene crustal extension of the Apennines (Italy). *Terra Nova*, 11 (2/3), 67-72. doi: 10.1046/j.1365-3121.1999.00227.

Goesele, M., Snavely, N., Curless, B., Hoppe, H., Seitz, S. M. (2007). Multi-view stereo for community photo collections. In: *2007 IEEE 11th International Conference on Computer Vision*, 1-8. IEEE.

Gosse, J. C., Phillips, F. M. (2001). Terrestrial in situ cosmogenic nuclides: theory and application. *Quaternary Science Reviews*, *20* (14), 1475-1560.

Guidoboni E., Ferrari G., Mariotti D., Comastri A., Tarabusi G., Sgattoni G., Valensise G. (2018). *CFTI5Med, Catalogo dei Forti Terremoti in Italia (461 aC-1997) e nell'area Mediterranea (760 aC-1500)*. Istituto Nazionale di Geofisica e Vulcanologia (INGV). http://storing.ingv.it/cfti/cfti5/.

Howle J. F., Bawden G. W., Schweickert R. A., Finkel R. C., Hunter L. E., Rose R. S., Twistern B. (2012). Airborne LiDAR analysis and geochronology of faulted glacial moraines in the Tahoe-Sierra frontal fault zone reveal substantial seismic hazards in the Lake Tahoe region, California-Nevada, USA. *GSA Bulletin*, 124 (7-8), 1087–1101. doi: 10.1130/B30598.1.

Improta L., Latorre D., Margheriti L., Nardi A., Marchetti A., Lombardi A. M., Castello B., Villani F., Ciaccio M. G., Mele F. M., Moretti M., The Bollettino Sismico Italiano Working Group (2019). Multi-segment rupture of the 2016 Amatrice-Visso-Norcia seismic sequence (central Italy) constrained by the first high-quality catalog of Early Aftershocks. Scientific reports, 9(1), 1-13.

James M. R., Robson S. (2012). Straightforward reconstruction of 3D surfaces and topography with a camera: Accuracy and geoscience application. *Journal of Geophysical Research: Earth Surface*, 117 (F3). doi: 10.1029/2011JF002289.

Jancosek, M., Shekhovtsov, A., Pajdla, T. (2009). Scalable multi-view stereo. In: *2009 IEEE 12th International Conference on Computer Vision Workshops*, ICCV Workshops, 1526-1533. IEEE.

Johnson K., Nissen E., Saripalli S., Arrowsmith J. R., McGarey P., Scharer K., Williams P., Blisniuk K., Blisniuk, K. (2014). Rapid mapping of ultrafine fault zone topography with structure from motion. *Geosphere*, 10 (5), 969-986. doi: 10.1130/GES01017.1.

Johnson K. L., Nissen E., Lajoie L. (2018). Surface rupture morphology and vertical slip distribution of the 1959 Mw 7.2 Hebgen Lake (Montana) earthquake from airborne lidar topography. *Journal of Geophysical Research: Solid Earth*, 123, 8229–8248. 10.1029/2017JB015039.

Kastelic V., Burrato P., Carafa M. M., Basili, R. (2017). Repeated surveys reveal nontectonic exposure of supposedly active normal faults in the central Apennines, Italy. *Journal of Geophysical Research: Earth Surface*, 122 (1), 114-129. doi: 10.1002/2016JF003953.

Klinger Y., Etchebes M., Tapponier P., Narteau C. (2011). Characteristic slip for five great earthquakes along the Fuyun Fault in China. *Nat. Geosci.*, 4, 389-392. doi:

10.1038/NGEO1158.

Koopman A. (1983). Detachment tectonics in the central Apennines, Italy. *Geol. Ultraiectina*, 30, 1-55.

Lavecchia G. (1985). Il sovrascorrimento dei Monti Sibillini: analisi cinematica e strutturale. *Boll. Soc. Geol. Ital.*, 104 , 161-194.

Lavecchia G., Brozzetti F., Barchi M., Menichetti M., Keller J. V. A. (1994). Seismotectonic zoning in east-central Italy deduced from an analysis of the Neogene to present deformations and related stress fields. *Geological Society of America Bulletin*, 106 (9), 1107–1120. doi: 10.1130/0016-7606(1994)106<1107:SZIECI>2.3.CO;2.

Leonard M. (2010). Earthquake fault scaling: Self-consistent relating of rupture length, width, average displacement, and moment release. *Bulletin of the Seismological Society of America*, 100 (5A), 1971–1988. doi: 10.1785/0120090189.

Livio F. A., Michetti A. M., Vittori E., Gregory L., Wedmore L., Piccardi L., Tondi E., Roberts Gerald P., Blumetti A.M., Bonadeo L., Brunamonte F., Comerci V., Dimanna P., Ferrario M. F., Faure Walker J., Frigerio C., Fumanti F., Guerrieri L., Iezzi F., Leoni G., McCaffrey K., Mildon Z., Phillips R., Rhodes E., Walters R. J., Wilkinson M. (2016) Surface faulting during the August 24, 2016, central Italy earthquake (Mw 6.0): preliminary results. *Annals of Geophysics*, 59 (5), ISSN 2037-416X.

Machette M. N., Pierce K. L., McCalpin J. P., Haller K. M., Dart R. L., (2001). Map and Data for Quaternary Faults and Folds in Wyoming. *U.S. Geological Survey Open-File Report*, 01–461, p. 153.

Manighetti I., Perrin C., Dominguez S., Garambois S., Gaudemer Y., Malavieille J., Matteo L., Delor E., Vitard C., Beauprêtre, S. (2015). Recovering paleoearthquake slip record in a highly dynamic alluvial and tectonic region (Hope Fault, New Zealand) from airborne lidar. *J. Geophys. Res. Solid Earth*, 120, 4484–4509. doi: 10.1002/2014JB011787.

McCalpin J. P. (2009). *Paleoseismology*. 2nd Edition, Academic Press, Amsterdam-London, pp. 615 (International Series, 95).

Michetti A. M., Brunamonte F., Serva L., Vittori, E. (1996). Trench investigations of the 1915 Fucino earthquake fault scarps (Abruzzo, central Italy): Geological evidence of large historical

events. *Journal of Geophysical Research*, 101 (B3), 5921–5936. doi: 10.1029/95JB02852.

Mildon Z. K., Roberts G. P., Walker J. P. F., Wedmore L. N., McCaffrey K. J. (2016). Active normal faulting during the 1997 seismic sequence in Colfiorito, Umbria: Did slip propagate to the surface? *Journal of Structural Geology*, 91, 102-113. doi: 10.1016/j.jsg.2016.08.011.

Mirabella F., Barchi M., Lupattelli A., Stucchi E., Ciaccio M. G. (2008). Insights on the seismogenic layer thickness from the upper crust structure of the Umbria-Marche Apennines (central Italy). *Tectonics*, 27 (1), doi: 10.1029/2007TC002134.

Morewood N. C., Roberts G. P. (2000). The geometry, kinematics and rates of deformation within an en échelon normal fault segment boundary, central Italy. *Journal of Structural Geology*, 22 (8), 1027-1047. doi: 10.1016/S0191-8141(00)00030-4

Oddone E. (1915). Gli elementi fisici del grande terremoto marsicano-fucense del 13 gennaio 1915. *Bollettino Società Geologica Italiana,* 19, 71–216.

Palumbo L., Benedetti L., Bourlès D., Cinque A., Finkel R. (2004). Slip history of the Magnola fault (Apennines, central Italy) from 36Cl surface exposure dating: evidence for strong earthquake over the Holocene. *Earth Planet. Sci. Lett.*, 225, 163–176.

Pantosti, D., D'Addezio, G., Cinti, F. R. (1996). Paleoseismicity of the Ovindoli-Pezza fault, central Apennines, Italy: A history including a large, previously unrecorded earthquake in the Middle Ages (860–1300 AD). *Journal of geophysical research: solid earth*, 101(B3), 5937-5959.

Papanikolaou I. D., Roberts G. P., Michetti A. M. (2005). Fault scarps and deformation rates in Lazio–Abruzzo, Central Italy: Comparison between geological fault slip-rate and GPS data. *Tectonophysics*, 408 (1-4), 147-176. doi: 10.1016/j.tecto.2005.05.043.

Piccardi L., Gaudemer Y., Tapponnier P., Boccaletti M. (1999). Active oblique extension in the central Apennines (Italy): evidence from the Fucino region. *Geophysical Journal International*, 139 (2), 499-530. doi: 10.1046/j.1365-246x.1999.00955.x.

Pierantoni P. P., Deiana G., Romano A., Paltrinieri W., Borraccini F., Mazzoli S. (2005). Geometrie strutturali lungo la thrust zone del fronte montuoso umbro-marchigiano-sabino. *Bollettino della Società geologica italiana*, 124 (2), 395-411.

Pierantoni P. P., Deiana G., Galdenzi, S. (2013). Geological map of the Sibillini Mountains (Umbria-

Marche Apennines, Italy). *Italian Journal of Geosciences*, 132 (3), 497–520.

Pierce K. L., Good J. D. (1992). Field guide to the quaternary geology of Jackson Hole, Wyoming. *U.S. Geological Survey Open-File Report*, 92-504. doi: 10.3133/ofr92504.

Pizzi A., Galadini F. (2009). Pre-existing cross-structures and active segmentation in the northern-central Apennines (Italy). *Tectonophysics*, 476, 304–319. doi: 10.1016/j.tecto.2009.03.018.

Pizzi A., Calamita F., Coltorti M., Pieruccini P. (2002). Quaternary normal faults, intramontane basins and seismicity in the Umbria-Marche-Abruzzi Apennine Ridge (Italy): Contribution of neotectonic analysis to seismic hazard assessment. *Bollettino Società Geologica Italiana*, Special Issue, 1, 923–929.

Pizzi A., Di Domenica A., Gallovič F., Luzi L., Puglia R. (2017). Fault segmentation as constraint to the occurrence of the main shocks of the 2016 central Italy seismic sequence. *Tectonics*, 36, 2370–2387. doi: 10.1002/2017TC004652.

Porreca M., Fabbrizzi, A. Azzaro, S., Pucci S., Del Rio L., Pierantoni P. P., Giorgetti C., Roberts G., Barchi M. R.. (2020). 3D geological reconstruction of the M. Vettore seismogenic fault system (Central Apennines, Italy): Cross-cutting relationship with the M. Sibillini thrust. *Journal of Structural Geology*, 131, 103938. doi: 10.1016/j.jsg.2019.103938.

Pucci S., De Martini P. M., Civico R. Villani F., Nappi R., Ricci T., Azzaro R., Brunori C. A., Caciagli M., Cinti F. R., Sapia V., De Ritis R., Mazzarini F., Tarquini S., Gaudiosi G., Nave R., Alessio G. Smedile A., Alfonsi L., Cucci L., Pantosti D. (2017). Coseismic ruptures of the 24 August 2016, Mw 6.0 Amatrice earthquake (central Italy). *Geophysical Research Letters*, 44 (5), 2138–2147. doi: 10.1002/2016GL071859.

Puliti I., Pizzi A., Benedetti L., Di Domenica A., Fleury J. (2020). Comparing slip distribution of an active fault system at various timescales: Insights for the evolution of the Mt. Vettore-Mt. Bove fault system in Central Apennines. *Tectonics*, 39 (9), e2020TC006200, doi: 10.1029/2020TC006200.

Ren Z. K., Zhang Z. Q., Chen T., Yan S. L., Yin J. H., Zhang P. Z., Zheng W. J., Zhang H. P., Li C. Y. (2016). Clustering of offsets on the Haiyuan Fault and their relationship to paleoearthquakes. *Geol. Soc. Am. Bull.*, 128 (1–2), 3–18. doi: 10.1130/B31155.1.

Roberts G. P., Michetti A. M. (2004). Spatial and temporal variations in growth rates along active

normal fault systems: an example from The Lazio–Abruzzo Apennines, central Italy. *Journal of Structural Geology*, 26 (2), 339-376. doi: 10.1016/S0191-8141(03)00103-2.

Roberts G. P., Cowie P., Papanikolou I., Michetti A. M. (2004). Fault scaling relationships, deformation rates and seismic hazards: An example from the Lazio–Abruzzo Apennines, central Italy. *Journal of Structural Geology*, 26 (2), 377–398. doi: 10.1016/S0191-8141(03)00104-4.

Rovida A., Locati M., Camassi R., Lolli B., Gasperini P. (Eds.) (2016). *CPTI15, the 2015 version of the parametric catalogue of Italian earthquakes. Istituto Nazionale di Geofisica e Vulcanologia*. doi: 10.6092/INGV.IT-CPTI15.

Sapia, V., Villani, F., Fischanger, F., Lupi, M., Baccheschi, P., Pantosti, D., Pucci, S., Civico, R., Sciarra, A., Smedile, A., Romano, P., De Martini, P.M., Mugia, F., Materni, V., Giannattasio, F., Pizzimenti, L., Ricci, T., Brunori, C.A., Coco, I., Improta, L., (2021). 3-D deep electrical resistivity tomography of the major basin related to the 2016 Mw 6.5 central Italy earthquake fault. *Tectonics*, doi: 10.1029/2020TC006628.

Salisbury J. B., Rockwell T. K., Middelton T. J., Hudnut K. W. (2012). Lidar and field observations of slip distribution for the most recent surface ruptures along the Central San Jacinto Fault *Bull. Seismol. Soc. Am.*, 102 (2), 598-619, doi: 10.1785/0120110068.

Scotti O., Visini F., Faure Walker J., Peruzza L., Pace B., Benedetti L., Boncio P., Roberts G. (2021). Which fault threatens me most? Bridging the gap between geologic data-providers and seismic risk practitioners. *Frontiers in Earth Science*, 8, 750, doi: 10.3389/feart.2020.626401.

Serva L., Blumetti A. M., Michetti A. M., (1988), Gli effetti sul terreno del terremoto del Fucino (13.01.1915); tentativo di interpretazione della evoluzione tettonica recente di alcune strutture. *Mem. Soc. Geol. Ital.*, 35, 893-907, 1988.

Schlagenhauf A., Gaudemer Y., Benedetti L., Manighetti I., Palumbo L., Schimmelpfennig I., Finkel R., Pou K. (2010). Using in situ Chlorine-36 cosmonuclide to recover past earthquake histories on limestone normal fault scarps: a reappraisal of methodology and interpretations. *Geophysical Journal International*, 182 (1), 36-72, doi: 10.1111/j.1365-246X.2010.04622.x.

Schlagenhauf, A., I. Manighetti, L. Benedetti, Y. Gaudemer, R. Finkel, J.Malavieille, and K. Pou (2011). Earthquake supercycles in central Italy, inferred from 36Cl exposure dating. *Earth*

Planet. Sci. Lett., 307, 487–500.

Scholz C. H., Dawers N. H., Yu J. Z., Anders M. H., Cowie P. (1993). Fault growth and fault scaling laws: Preliminary results. *Journal of Geophysical Research*, 98 (B12), 21,951–21,961. doi: 10.1029/93JB01008.

Scognamiglio L., Tinti E., Casarotti E., Pucci S., Villani F., Cocco M., Magnoni F., Michelini A., Dreger D. (2018). Complex fault geometry and rupture dynamics of the MW 6.5, 30 October 2016, central Italy earthquake. *Journal of Geophysical Research: Solid Earth*, 123 (4), 2943-2964. doi: 10.1002/2018JB015603.

Serpelloni E., Anzidei,M., Baldi P., Casula G., Galvani A. (2005). Crustal velocity and strain-rate fields in Italy and surrounding regions: new results from the analysis of permanent and non-permanent GPS networks. *Geophysical Journal International*, 161, 861-880. doi:10.1111/j.1365-246X.2005.02618.x.

Smith R. B., Byrd J. O., Susong D. D. (1993). The Teton fault, Wyoming: Seismotectonics, Quaternary history, and earthquake hazards. *Geology of Wyoming: Geological Survey of Wyoming Memoir*, 5, 628-667.

Smith R. B., Siegel, L. J. (2000). *Windows into the Earth: The Geologic Story of Yellowstone and Grand Teton National Parks*, 242 p.

Stirling M., Goded T., Berryman K., Litchfield N. (2013). Selection of earthquake scaling relationships for seismic-hazard analysis. *Bulletin of the Seismological Society of America*, 103 (6), 2993–3011. doi: 10.1785/0120130052.

Schwartz D. P., Coppersmith K. J. (1984). Fault behavior and characteristic earthquakes: examples from the Wasatch and San Andreas fault zones. *J. Geophys. Res.*, 89 (B7), 5681-5698.

Tondi E., Cello G. (2003). Spatiotemporal evolution of the Central Apennines fault system (Italy). *Journal of Geodynamics*, 36 (1-2), 113-128. doi: 10.1016/S0264-3707(03)00043-7.

Tinti E., Scognamiglio L., Michelini A., Cocco M. (2016). Slip heterogeneity and directivity of the ML 6.0, 2016, Amatrice earthquake estimated with rapid finite-fault inversion. *Geophysical Research Letters*, 43, 10,745–10,752. doi: 10.1002/2016GL071263.

Tucker, G. E., McCoy, S. W., Whittaker, A. C., Roberts, G. P., Lancaster, S. T., Phillips, R. (2011). Geomorphic significance of postglacial bedrock scarps on normal-fault footwalls. *Journal*

of Geophysical Research: Earth Surface, 116 (F1), doi: 10.1029/2010JF001861.

Vai G. B., Martini I. P. (Eds.) (2001). *Anatomy of an Orogen: The Apennines and adjacent mediterranean basins*. Dordrecht, Netherlands: Kluwer Acad. pp. 633, doi: 10.1007/978-94-015-9829-3.

Vezzani L., Festa A., Ghisetti F. C. (2010). Geology and tectonic evolution of the Central-Southern Apennines, Italy. *Geological Society of America, Special Paper,* 469, 1-58, doi:10.1130/2010.2469.

Villani F., Civico R., Pucci S., Pizzimenti L., Nappi R., De Martini P. M., and the Open EMERGEO Working Group (2018). A database of the coseismic effects following the 30 October 2016 Norcia earthquake in central Italy. *Scientific Data*, 5, 180,049. doi: 10.1038/sdata.2018.49.

Villani F., Pucci S., Civico R., De Martini P. M., Cinti F. R., Pantosti D. (2018). Surface faulting of the 30 October 2016 Mw 6.5 central Italy earthquake: Detailed analysis of a complex coseismic rupture. *Tectonics*, 37 (10), 3378-3410. doi: 10.1029/2018TC005175.

Villani F., Sapia V., Baccheschi P., Civico R., Di Giulio G., Vassallo M., Marchetti M., Pantosti D. (2019). Geometry and structure of a fault-bounded extensional basin by integrating geophysical surveys and seismic anisotropy across the 30 October 2016 Mw 6.5 earthquake fault (central Italy): The Pian Grande di Castelluccio basin. *Tectonics*, 38 (1), 26-48. doi: 10.1029/2018TC005205.

Vittori E., Di Manna P., Blumetti A. M., Comerci V., Guerrieri L., Esposito E. Michetti A. M., Porfido S., Piccardi L., Roberts G. P., Berlusconi A., Livio F., Sileo G., Wilkinson M., McCaffrey K. J. W., Phillips R. J., Cowie P. A. (2011). Surface Faulting of the 6 April 2009 Mw 6.3 L'Aquila Earthquake in Central Italy. Bulletin of the Seismological Society of America ; 101 (4): 1507–1530. doi: https://doi.org/10.1785/0120100140Surface faulting of the 6 April 2009 Mw 6.3 L'Aquila earthquake in central Italy. *Bulletin of the Seismological Society of America*, 101 (4), 1507–1530. doi: 10.1785/0120100140

Wallace R. E. (1968). Earthquake of August 19, 1966, Varto Area, eastern Turkey. *Bulletin of the Seismological Society of America*, 58 (1), 11–45.

Wallace R. E. (1977). Profiles and ages of young fault scarps, north-central Nevada. *Geological Society of America Bulletin*, 88 (9), 1267-1281.

Wells, D. L., Coppersmith, K. J. (1994). New empirical relationships among magnitude, rupture length, rupture width, rupture area, and surface displacement. *Bulletin of the seismological Society of America*, 84 (4), 974-1002.

Westoby M., Brasington J., Glasser N. F., Hambrey M. J., Reynolds J. M. (2012). Structure-from-Motion photogrammetry: A novel, low-cost tool for geomorphological applications. *Geomorphology*, 179, 300-314. doi:10.1016/j.geomorph.2012.08.021.

Wiatr T., Papanikolaou I., Fernández-Steeger T., Reicherter K. (2015). Bedrock fault scarp history: insight from t-LiDAR backscatter behaviour and analysis of structure changes. *Geomorphology*, 228, 421-431.

Wilkinson M. W., McCaffrey K. J. W., Jones R. R., Roberts G. P., Holdsworth R. E., Gregory L. C., Walters R. J., Wedmore L., Goodall H., Iezzi F. (2017). Near-field fault slip of the 2016 Vettore Mw 6.6 earthquake (central Italy) measured using low-cost GNSS. *Scientific Reports*, 7 (1), 4612. doi: 10.1038/s41598-017-04917-w.

Zielke O., Arrowsmith J. R., Grant Ludwig L., Akçiz S. O. (2010). Slip in the 1857 and earlier large earthquakes along the Carrizo Plain, San Andreas Fault. *Science*, 327, 1119, doi: 10.1126/science.1182781.

Zielke O., Arrowsmith J. R., Grant Ludwig L., Akçiz S. O. (2012). High-resolution topography-derived offsets along the 1857 Fort Tejon Earthquake Rupture Trace, San Andreas Fault. *Bull. Seismol. Soc. Am.*, 102 (3), 1,135-1,154, doi: 10.1785/0120110230.

Supplementary materials

High resolution morphometric analysis of the Cordone del Vettore normal fault scarp (2016 central Italy seismic sequence): insights into age, earthquake recurrence and throw rates

S. Pucci[a], L. Pizzimenti[a], R. Civico[a], F. Villani[a], C. A. Brunori[a] and D. Pantosti[a]

[a]Istituto Nazionale di Geofisica e Vulcanologia, via di Vigna Murata 605, 00143 Rome, Italy.

Corresponding author: Stefano Pucci, stefano.pucci@ingv.it

Availability of data and codes:

Photoset and point cloud used for the CDV DSM and derivatives production will be provided on request.

CDV DSM, Excel spreadsheet of sampling points and Python codes are included as electronic material.

S1. DSM production

GCP Label	Longitude	Latitude	Altitude	Error (m)	X error (m)	Y error (m)	Z error (m)	Lon estimate	Lat estimate	Altitude estimate
point 2	13,260893	42,8119	2109,7991	0,010462	-0,00166	-0,00756	0,007044	13,26089	42,8119	2109,806
point 3	13,255548	42,816247	2207,0583	0,114636	0,073036	0,081925	0,033095	13,25555	42,81625	2207,091
point 5	13,246909	42,821982	2001,2874	0,241757	0,010987	-0,22321	0,092213	13,24691	42,82198	2001,38
point 6	13,248893	42,82187	2094,9926	0,422297	0,332928	-0,01925	0,259081	13,2489	42,82187	2095,252
point 7	13,250647	42,820272	2144,3854	0,451335	-0,38183	-0,06031	-0,23296	13,25064	42,82027	2144,152
point 9	13,247444	42,823672	2051,3721	0,171793	-0,11562	0,125236	0,02146	13,24744	42,82367	2051,394

point 10	13,245766	42,823426	1979,6978	0,465645	0,444602	-0,01658	-0,1374	13,24577	42,82343	1979,56
point 11	13,247203	42,824294	2044,731	0,165884	-0,08166	0,113807	-0,08887	13,2472	42,8243	2044,642
point 12	13,246997	42,824661	2041,2176	0,116727	-0,08813	-0,06794	-0,03524	13,247	42,82466	2041,182
point 13	13,246662	42,825223	2031,4717	0,284902	-0,23886	-0,15477	-0,01282	13,24666	42,82522	2031,459
point 14	13,245502	42,826164	1994,5231	0,436324	-0,356	0,125267	0,218971	13,2455	42,82617	1994,742
point 15	13,24654	42,827284	2064,5818	0,419215	-0,10006	0,308101	-0,26609	13,24654	42,82729	2064,316
point 16	13,246811	42,82841	2093,0355	0,876204	0,810568	-0,17863	0,28072	13,24682	42,82841	2093,316
point 17	13,246447	42,829351	2078,739	0,227885	-0,16447	0,037274	-0,15327	13,24645	42,82935	2078,586
point 18	13,24684	42,831045	2065,1515	0,180772	-0,16272	-0,07456	-0,02535	13,24684	42,83104	2065,126
point 22	13,250658	42,833921	2313,3209	0,070724	0,029689	0,003817	0,064078	13,25066	42,83392	2313,385
#Total error				0,328141	0,27075	0,11867	0,142437			

Table S1. Difference between GCPs and estimated marker positions as exported from the reference pane of Agisoft Photoscan Pro® (v. 1.4.5).

S2. Data extraction workflow

The profile extraction process was carried out within the GIS QGIS 2.18 environment through the Swath Profile plugin. 864 profiles, 1 m-spaced, were traced orthogonal to the average direction of the fault scarps (257°N and 234°N, for Sector 1 and 2, respectively). By means of the VOGIS Tool plugin, we assigned the attributes of Slope and Elevation values to each profile, converting each profile line in 0.5 m-spaced points. Then, according to the slope values changes, the profiles were cut at the scarp base, providing the along-strike baseline. Each profile ("Scarp

profile" sheet in Pucci_2021Geom_data.xlsx) is therefore tagged by a Profile Number, corresponding to the progressive distance from the starting profile, and along each profile the Points Number are upslope tagged, providing the distance from the baseline ("Erosional surface" sheet in Pucci_2021Geom_data.xlsx). The Near (Analysis) ArcGIS geoprocessing tool was used to assign the field-measured fault dip angle (α) values to the scarp baseline. Then, using Excel and Python (in Supplementary Electronic Material) and, in particular, the Pandas module (Scarp_codes.rar in Supplementary Electronic Material), it was possible to extract the variable necessary to calculate the minimum throw according to the Eq. 1. The envelope of the footwall erosional surface was defined on the profiles set through a simple linear regression method using the SciPy module in Python, providing the slope γ, the intercept (surface offset S) and related statistical data (Erosional_Surface_regressions.rar in Supplementary Electronic Material).

All the data were organized in the "Pucci_2021Geom_data.xlsx" spreadsheet (in Supplementary Electronic Material), containing the data fields of Tabs. S2.1 and S2.2.

FID	Profile Number	Distance along scarp baseline (m)	Point Number per profile	Lon (UTM 33 wgs84)	Lat (UTM 33 wgs84)	Slope (°)	Elev (m)	Along-profile distance (m)	Elevation from baseline (m)

Table S2.1. Header of "Scarp profile" sheet in Pucci_2021Geom_data.xlsx with data of the 0.5 m-spaced points forming each profile on both footwall erosional surface sectors.

Profile Number	Distance along scarp baseline (m)	Longitude (UTM 33 wgs84), scarp baseline	Longitude (UTM 33 wgs84), scarp baseline	Elevation (m a.s.l.), scarp baseline	Profile Length (m)	Fault Plane Dip Angle (α, °)	Fault Plane Dip Angel (α, rad)
tan(α)	γ	tan(γ)	y intercept (m a.s.l.)	R^2	Standard error	Surface Offset (m)	Minimum Throw (m)

Table S2.2. Header of “Erosional surface” sheet in Pucci_2021Geom_data.xlsx with data used in the calculation of minimum throw distribution profile along the CDF scarp for each profile.